



Wave-equation-based travel-time seismic tomography – Part 2: Application to the 1992 Landers earthquake (M_w 7.3) area

P. Tong¹, D. Zhao², D. Yang³, X. Yang⁴, J. Chen⁴, and Q. Liu¹

¹Department of Physics, University of Toronto, Toronto, M5S 1A7, Ontario, Canada

²Department of Geophysics, Tohoku University, Sendai, Japan

³Department of Mathematical Sciences, Tsinghua University, Beijing, China

⁴Department of Mathematics, University of California, Santa Barbara, California, USA

Correspondence to: P. Tong (tongping85@gmail.com)

Received: 10 August 2014 – Published in Solid Earth Discuss.: 25 August 2014

Revised: 19 October 2014 – Accepted: 24 October 2014 – Published: 26 November 2014

Abstract. High-resolution 3-D P and S wave crustal velocity and Poisson's ratio models of the 1992 Landers earthquake (M_w 7.3) area are determined iteratively by a wave-equation-based travel-time seismic tomography (WETST) technique. The details of data selection, synthetic arrival-time determination, and trade-off analysis of damping and smoothing parameters are presented to show the performance of this new tomographic inversion method. A total of 78 523 P wave and 46 999 S wave high-quality arrival-time data from 2041 local earthquakes recorded by 275 stations during the period of 1992–2013 are used to obtain the final tomographic models, which cost around 10 000 CPU hours. Checkerboard resolution tests are conducted to verify the reliability of inversion results for the chosen seismic data and the wave-equation-based travel-time seismic tomography method. Significant structural heterogeneities are revealed in the crust of the 1992 Landers earthquake area which may be closely related to the local seismic activities. Strong variations of velocity and Poisson's ratio exist in the source regions of the Landers and three other nearby strong earthquakes. Most seismicity occurs in areas with high-velocity and low Poisson's ratio, which may be associated with the seismogenic layer. Pronounced low-velocity anomalies revealed in the lower crust along the Elsinore, the San Jacinto, and the San Andreas faults may reflect the existence of fluids in the lower crust. The recovery of these strong heterogeneous structures is facilitated by the use of full wave equation solvers and WETST and verifies their ability in generating high-resolution tomographic models.

1 Introduction

In Tong et al. (2014b) (hereinafter referred to as paper I), we introduced a new tomographic method, the so called wave-equation-based travel-time seismic tomography (WETST) which is a “2-D–3-D” adjoint tomography technique based upon a high-order finite-difference solver. This approach restricts each forward modeling in a 2-D vertical plane containing the source and the receiver, while tomographic unknowns such as velocity perturbations are specified on a 3-D inversion grid. Comparing with the “3-D–3-D” wave-equation travel-time inversion (Luo and Schuster, 1992) or the “3-D–3-D” adjoint tomography based on spectral-element numerical solvers (e.g., Tromp et al., 2005; Fichtner et al., 2006; Tape et al., 2009), the theoretical disadvantage of this “2-D–3-D” tomographic method is that it ignores the influence of the off-plane structures on seismic arrivals. However, from the computational aspect, WETST is generally much more efficient. This is essential for tomographic problems involving large data sets, which is important for increasing the illumination of subsurface structures. Because the off-ray finite-frequency effects within the 2-D vertical plane are considered, WETST has a theoretical advantage over simple ray-based tomographic methods. In this second paper, we choose the 1992 Landers earthquake area as our study area and test the performance of WETST in a realistic application.

The 1992 Landers earthquake with a magnitude of 7.3 occurred on 28 June 1992 in the Mojave Desert of southern California (Fig. 1). The source area is also within the southern part of the eastern California shear zone, a major tectonic

element of the transform plate boundary zone between the Pacific and North America Plates (Sieh et al., 1993). The epicenter was located at 34.161° N, 116.396° W and its focal depth was 7.0 km (Zhao and Kanamori, 1993). This large earthquake had a right-lateral strike slip focal mechanism, agreeing with the regional deformation of the Mojave block (Unruh et al., 1994; Peyrat et al., 2001). It caused a surface rupture of approximate 80 km across a series of complex fault intersections (Unruh et al., 1994). More than 40 000 foreshocks, preshocks, and aftershocks to the Landers earthquake were reported by the Southern California Seismographic Network (SCSN) in the year 1992 (Sieh et al., 1993). The Landers earthquake sequence itself is the largest sequence recorded by SCSN since the monitoring began in 1920s (Hauksson et al., 1993). Besides the Landers mainshock, the Joshua Tree foreshock (M_w 6.1) and the Big Bear aftershock (M_w 6.2) are two other main events of this sequence (Fig. 1). The 1999 Hector Mine earthquake (M_w 7.1) which is considered to be triggered by the 1992 Landers earthquake is another large earthquake in the study area from the past 20 years (Parsons and Dreger, 2000). To gain insights into the earthquake sequences and local crustal heterogeneities, many researchers have investigated the Landers mainshock, the corresponding sequence, and the structures of the source area using different techniques (e.g., Hauksson et al., 1993; Zhao and Kanamori, 1993; Freymueller et al., 1994; Olsen et al., 1997; Aochi and Fukuyama, 2002). Seismic tomography has shown to be one of the most promising tools in revealing the heterogeneous structures of the Earth's interior (e.g., Thurber, 1983; Zhao, 2009; Rawlinson et al., 2010a; Liu and Gu, 2012). With the large number of high-quality seismic data recorded by SCSN, it is possible to explore the Landers earthquake area by tomographic techniques. Additionally, the detailed tomographic structures may then improve our understanding of the relationship between the occurrence of large crustal earthquakes and local structural heterogeneities (Zhao and Kanamori, 1993; Lin et al., 2007).

The seismic velocity structures beneath southern California have been investigated by numerous researchers (e.g., Zhao and Kanamori, 1993; Lin et al., 2007; Tian et al., 2007b; Tape et al., 2009, 2010; Allam and Ben-Zion, 2012). These tomographic results generally show that strong structural heterogeneities exist in the crust and upper mantle under southern California (e.g., Zhao et al., 1996; Tape et al., 2010). Furthermore, Lin et al. (2007) observed a weak correlation between earthquake occurrence and seismic velocities, with upper-crust earthquakes mostly occurring in high P velocity regions and mid-crustal earthquakes occurring in low P velocity regions. For the source area of the 1992 Landers earthquake, Zhao and Kanamori (1993) and Zhao et al. (2005) successively mapped out detailed P and S wave tomographic images, both of which showed strong heterogeneous velocity structures and suggested that the earthquake occurrence may be closely related to crustal heterogeneities. Lees and

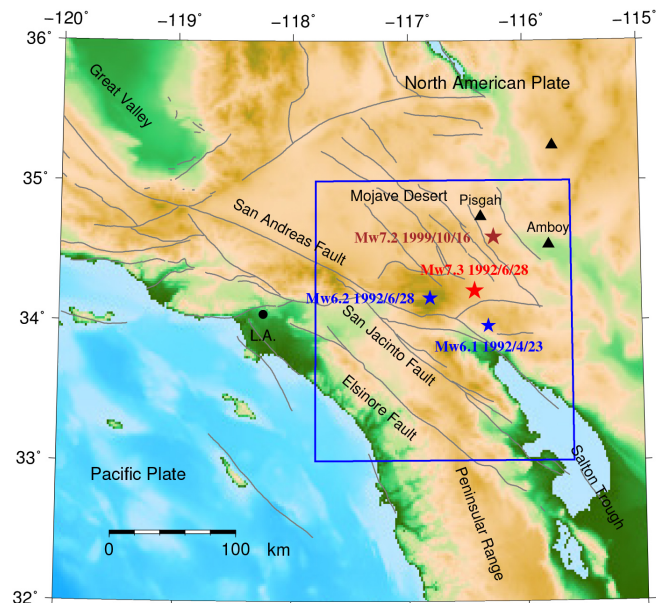


Figure 1. The tectonic conditions and surface topography around southern California. The blue box indicates the present study area. The red star represents the epicenter of the 1992 Landers earthquake ($M_w = 7.3$), the two blue stars show epicenters of the 1992 Joshua Tree earthquake ($M_w = 6.1$) and the 1992 Big Bear earthquake ($M_w = 6.2$), and the brown star denotes the epicenter of the 1999 Hector Mine earthquake ($M_w = 7.2$). Active regional faults and volcanic centers are indicated by grey curves and black triangles, respectively.

Nicholson (1993) reached the same conclusion through tomographic inversion of P wave arrival times from aftershocks of the 1992 Landers earthquake. Tian et al. (2007a) simultaneously determined P and S wave velocity and Poisson's ratio models for the Landers earthquake area. They showed a correlation between the seismic activity and crustal heterogeneities and suggested that the existence of crustal fluids may have weakened the fault zone and thus triggered the Landers earthquake.

Taking these previous tomographic results as references, we test the performance of WETST in imaging crustal structures of the Landers earthquake source area. The tomographic images inverted by WETST may help shed some new lights on local heterogeneous structures and the nucleation of large crustal earthquakes.

2 Practical implementation

Taking the 1992 Landers earthquake area as our test field, in this section we show the implement of WETST in real data applications. The detailed theory of the WETST method is fully presented in paper I, and only key results of paper I are summarized as follows.

Wave-equation-based travel-time seismic tomography is rooted in the following tomographic equation

$$T^{\text{obs}} - T^{\text{syn}} = \int_{\Omega} K(\mathbf{x}; \mathbf{x}_r, \mathbf{x}_s) \frac{\delta c(\mathbf{x})}{c(\mathbf{x})} d\mathbf{x}, \quad (1)$$

where T^{obs} is the arrival time of the interested seismic phase picked on recorded seismogram, $c(\mathbf{x})$ is the P or S velocity model based on which synthetic arrival time T^{syn} is calculated, and $K(\mathbf{x}; \mathbf{x}_r, \mathbf{x}_s)$ is the travel-time sensitivity kernel constructed based on the interactions of forward wavefield $u(t, \mathbf{x})$ and adjoint wavefield $q(t, \mathbf{x})$ by

$$K(\mathbf{x}; \mathbf{x}_r, \mathbf{x}_s) = - \int_0^T \left[2c^2(\mathbf{x}) \nabla q(T - \tau, \mathbf{x}) \cdot \nabla u(\tau, \mathbf{x}) \right] d\tau. \quad (2)$$

The forward wavefield $u(t, \mathbf{x})$ and adjoint wavefield $q(t, \mathbf{x})$ satisfy the forward and adjoint acoustic wave equations as

$$\frac{\partial^2 u(t, \mathbf{x})}{\partial t^2} = \nabla \cdot \left[c^2(\mathbf{x}) \nabla u(t, \mathbf{x}) \right] + f(t) \delta(\mathbf{x} - \mathbf{x}_s), \quad (3)$$

and

$$\frac{\partial^2 q(t, \mathbf{x})}{\partial t^2} = \nabla \cdot \left[c^2(\mathbf{x}) \nabla q(t, \mathbf{x}) \right] + \frac{w(T - t) [\partial u(T - t, \mathbf{x}) / \partial t]}{\int_0^T w(t) u(t) [\partial^2 u(t) / \partial t^2] dt} \delta(\mathbf{x} - \mathbf{x}_r), \quad (4)$$

where $f(t)$ is the source time function and $w(t)$ is the time window function used to isolate a particular seismic phase (such as first P or S arrival in this study). We assume that seismic waves propagate in the vertical plane which contains the source \mathbf{x}_s and receiver \mathbf{x}_r and satisfy 2-D acoustic wave Eq. (3). This 2-D approximation is mainly invoked to reduce computational cost and enable the use of as many seismic data as possible. Given a reference velocity model $c(\mathbf{x})$, the purpose of WETST is to find the relative velocity perturbation $\delta c(\mathbf{x})/c(\mathbf{x})$ which can be then used to obtain the updated model $c(\mathbf{x}) + \delta c(\mathbf{x})$ that best explains travel-time data T^{obs} . To this end, we select seismic phases to make measurements T^{obs} , recast tomographic Eq. (1) on a set of inversion grid nodes, and solve an optimization problem.

2.1 Data

Our initial data consist of P and S wave arrival times of local earthquakes recorded by the SCSN, compiled by the Southern California Earthquake Data Center and obtained through the Seismogram Transfer Program (<http://www.data.seec.org/research-tools/stp-index.html>). In the study area (blue box in Fig. 1), SCSN data analysts have picked the phase data (first P and S arrivals) of nearly 30 000 earthquakes

Table 1. The starting 1-D velocity model (m_0) used in this study.

Depth to surface (km)	P wave velocity (km s^{-1})	S wave velocity (km s^{-1})
0.0–2.0	4.800	2.775
2.0–5.5	5.800	3.353
5.5–16.0	6.300	3.642
16.0–29.2	6.700	3.873
> 29.2	7.800	4.509

with magnitudes between 2.0 and 4.0 occurring during a period from January 1992 to November 2013. Since it is very computationally intensive and also unnecessary to include all these events, we only choose a small subset of them for our tomographic inversion.

To ensure that the chosen seismic data illuminate the study region well, events and corresponding phase records are carefully selected based on the following six criteria: (1) to guarantee the quality of seismic data and validity of point source assumption for forward modeling, the magnitudes of the selected events should be within the range [2.0, 4.0]; (2) to reduce the influence of mislocation errors on tomographic inversion, we only choose events with more than 20 P and more than 10 S arrivals; (3) the focal depth of each chosen event is greater than 3.0 km; (4) to ensure that picking errors of selected phase data are within an acceptable range, the misfit between the observed arrival time and the synthetic arrival time in the 1-D reference model (discussed later) is required to be less than 1.0 s for P wave or 1.5 s for S wave; (5) to save on computation, we only use seismic records whose epicentral distances are less than 100 km; (6) to avoid event clustering and keep a uniform distribution of hypocenter locations, we divide the Landers earthquake source area (the blue box in Fig. 1) into $2 \text{ km} \times 2 \text{ km} \times 2 \text{ km}$ blocks and only choose one event in each block that is recorded by the maximal number of stations if it exists. As a result, our selected data set includes 78 523 first P wave and 46 999 first S wave arrival times recorded by 275 SCSN stations (Fig. 2b) for 2041 local earthquakes (Fig. 2a).

2.2 Model parameterization

The discrete form of tomographic Eq. (1) requires model parameterization. We first need to define the forward modeling grid for the calculation of travel-time kernel $K(\mathbf{x}; \mathbf{x}_r, \mathbf{x}_s)$ in Eq. (2). Since in this study the travel-time kernel $K(\mathbf{x}; \mathbf{x}_r, \mathbf{x}_s)$ is computed on the vertical plane passing through the source \mathbf{x}_s and the receiver \mathbf{x}_r by numerically solving the two acoustic wave Eqs. (3) and (4) using a finite-difference scheme (i.e., the high-order central difference method presented in the appendix of paper I), the forward modeling grid should be designed to suit 2-D finite-difference calculations. Usually, for a finite-difference calculation, the computational domain is divided into a uniform grid where the grid size is

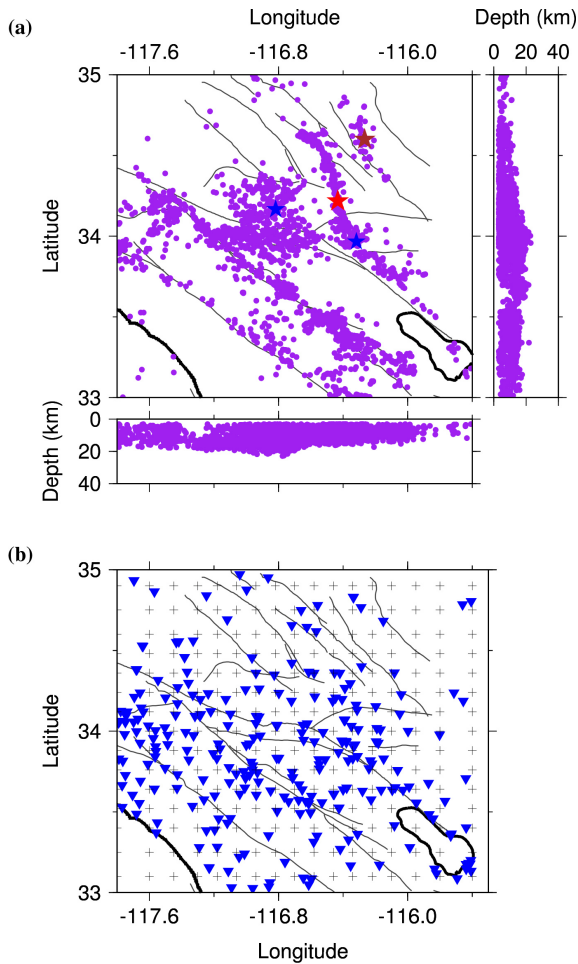


Figure 2. (a) Hypocentral distribution of the 2041 earthquakes (purple dots) used in this study. The stars denote the relatively large earthquakes which occurred in and around the Landers area as shown in Fig. 1. (b) Distribution of the 275 seismic stations (blue reverse triangles) used in this study. The grey crosses represent the inversion grid nodes.

determined by the velocity, dominant frequency of seismic wave, and stability condition of the numerical scheme.

We first define m_0 as a 1-D layered velocity model that contains five layers separated by two velocity boundaries at 2.0 km and 5.5 km, the Conrad discontinuity (16 km), and an averaged flat Moho (29.2 km) (Hauksson et al., 1993; Zhu and Kanamori, 2000). In each layer, the velocity structure is homogeneous and the corresponding P and S wave velocities are shown in Table 1. For this 1-D layered model, the arrival times of the direct P and S waves, head waves refracted from the velocity boundary at the depth of 5.5 km observed at epicentral distances > 40 –50 km, head wave (P^* , S^*) refracted from the Conrad discontinuity when the epicentral distances are in the range of 90–140 km, and head waves (Pn , Sn) from the Moho when the epicentral distances are greater than 140–150 km can be easily calculated accord-

ing to the geometrical ray theory (Zhao et al., 1992, 1996; Tong et al., 2011). Accordingly, the synthetic first P and S arrival times can be determined for each source–receiver pair based on its epicentral distance for the velocity model m_0 . However, the undulated Moho of southern California region has large lateral depth variation and strong influence on seismic wave propagation (Zhu and Kanamori, 2000), and has considerable effects on the tomographic images of the lower crust and the uppermost mantle (e.g., Zhao et al., 2005; Tian et al., 2007b). Therefore, for this study, we take into account the variation of Moho topography, and introduce a velocity model m_1 that differs m_0 by adding an undulated Moho obtained from receiver functions by Zhu and Kanamori (2000) as the starting model. The synthetic travel times of the first P and S waves in m_1 can be calculated by the combined ray and cross-correlation technique discussed in Paper I. Once the synthetic arriving times for m_1 and the observed arrival times picked from data are available, velocity structures can be updated from m_1 based on the WETST technique.

For the 2-D finite-difference forward modeling, we choose a Gaussian wavelet as the source time function $f(t)$ in Eq. (3)

$$f(t) = A \left[2\pi^2 f_0^2 \left(t - \frac{1.2}{f_0} \right)^2 - 1 \right] \exp \left(-\pi^2 f_0^2 \left(t - \frac{1.2}{f_0} \right)^2 \right), \quad (5)$$

where A is the amplitude and f_0 is the dominant frequency. The frequency spectrum of the source time function Eq. (5) is mainly concentrated within $[0, 2.5 f_0]$. For example, the spectrum (shown in Fig. 3b) for a $f(t)$ with unit amplitude $A = 1.0$ and dominant frequency $f_0 = 2.0$ Hz (Fig. 3a) has significant values between 0.0 Hz and 5.0 Hz. Correspondingly for consistency, data traces need to be filtered between the frequency range of $[0, 2.5 f_0]$ for the picking of observed travel times. We specifically denote the observed travel times picked on band-pass filtered seismograms as $T^{\text{obs},f}$. Since seismic waves filtered at different frequencies have different sensitivity to heterogeneous structures, arrival-time $T^{\text{obs},f}$ is not necessarily equal to T^{obs} obtained from the travel-time data catalog (such as the SCSN). We relate the two arrival times using the formula

$$T^{\text{obs},f} = T^{\text{obs}} + \delta t^f. \quad (6)$$

Fortunately, δt^f s are found to be very small and negligible in this study. In detail, we first choose the dominant frequencies $f_0 = 2.0$ Hz for P waves and $f_0 = 1.2$ Hz for S waves, since the dominant parts of the seismic energy are around these frequencies for moderate crustal earthquakes (e.g., Gautier et al., 2008; Tong et al., 2011). The wavelengths of the P wave are approximately equal to those of the S wave in the same layers. To explore the properties of the arrival-time difference δt^f in Eq. (6), a Butterworth filter between 0.001 Hz and 5.0 Hz is applied to more than

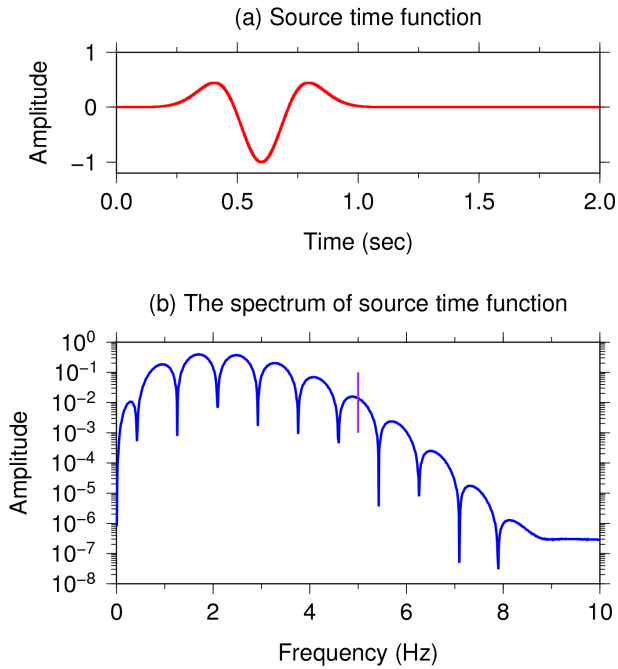


Figure 3. Panel (a) shows source time function Eq. (5) with unit amplitude $A = 1.0$ and dominant frequency $f_0 = 2.0$. Panel (b) shows frequency spectrum for the source time function in (a). The purple line is at 5.0 Hz.

50 arbitrarily selected P wave seismograms recorded for 10 earthquakes with magnitudes between 2.08 and 3.99. Figure 4 shows three such examples of T^{obs} and $T^{\text{obs},f}$ picked on raw and filtered seismograms. In all our selected examples we find that the differences δt^f are generally smaller than 0.08 s, which account for the combined effect of finite-frequency measurements, noise, and picking inaccuracy. For a regional P wave tomography as in this study, δt^f less than 0.08 s has very limited effect on the final images and can be safely viewed as noise, which will also be confirmed in the checkerboard resolution tests shown in the Supplement (Figs. S1 and S2). Similarly, δt^f can also be ignored for the S wave seismograms. Therefore, we would rather use the existing SCSN catalog of T^{obs} than hand-picking large number of $T^{\text{obs},f}$ for this tomographic study. In addition, the spacing of the uniform forward modeling grid is $\Delta x = \Delta z = 0.2$ km. The time steps are chosen to be $\Delta t = 0.0025$ s for P wave simulations and $\Delta t = 0.004$ s for S wave modelings. These parameters guarantee the stability condition of the high-order central difference method (Tong et al., 2014b).

One of the main purposes of forward modeling is to compute the sensitivity kernel as in Eq. (2). Prior to that, we need to determine the time window for the first arriving P -phase or S -phase. Since the onset time T^{syn} of a specific phase in an iterative model can be calculated by using the combined ray and cross-correlation method and the signal length (dependant on the source time Eq. 5) is about twice

the dominant period, the time window for the synthetic seismic phase is chosen to be $[T^{\text{syn}}, T^{\text{syn}} + 2.0/f_0]$. For the 1-D layered model with an undulated Moho (m_1) and at epicentral distances less than 100 km, the first P or S wave arrival of a crustal earthquake (depth greater than 3.0 km) should be either the direct phase Pg (Sg), head waves refracted from the velocity boundary at the depth of 5.5 km, or head waves P^* (S^*) refracted from the Conrad discontinuity depending on the epicentral distance. Accordingly, the travel-time sensitivity kernels for the first arrivals also have different spatial variations. Figures 5a, b and 6a, b show two typical sensitivity kernels for the velocity model m_1 . For example, the kernels of Pg and Sg waves at a distance of 3.75 km for an earthquake at the depth 3.14 km (Fig. 5a and b) clearly display 2-D cigar shapes (e.g., Tromp et al., 2005; Tape et al., 2007). On the synthetic seismograms (Fig. 5c and d), the direct Pg (Sg) and the reflected phase Pr (Sr) from the velocity boundary at 5.5 km are distinguishable and almost totally separated, which enables us to separate the direct arrivals and calculate their kernels (Fig. 5a and b). The negative kernel values in the first Fresnel zone indicate that a velocity decrease is required to delay the synthetic arrival time T^{syn} . However, for the records of 2041 selected crustal events, it is only possible to separate the first arrival from its coda waves on a very small fraction of synthetic seismograms. For many synthetic seismograms, the first arrivals are closely followed or even overlapped by other phases. For example, on the synthetic seismograms generated by the same crustal earthquake but recorded at a distance of 87.24 km (Fig. 6c and d), the first arrival Ph (Sh) refracted from the velocity boundary at 5.5 km depth is sequentially overlapped by the direct arrival Pg (Sg), the Conrad refracted phase P^* (S^*), and the reflected wave Pr (Sr) from the velocity boundary at 5.5 km depth. It is difficult to separate these phases because the later phases are in the time window of the first P wave (S wave) arrival. Therefore, the computed sensitivity kernels (Fig. 6a and b) have significant values around the traveling paths of all the phases that arrive within the first-arrival windows. This feature is helpful for resolving multipathing problems which are common for complex velocity structures (Rawlinson et al., 2010b). Every P wave/ S wave travel-time sensitivity kernel is also smoothed out by a Gaussian function with the scaling length chosen to be the minimum P wave/ S wave wavelength in the starting model m_1 (Tape et al., 2007; Tong et al., 2014a, b). Additionally, the sensitivity kernel $K(\mathbf{x}; \mathbf{x}_r, \mathbf{x}_s)$ and the relative velocity perturbation $\delta c(\mathbf{x})/c(\mathbf{x})$ are bilinearly interpolated on the forward modeling grid (Tong et al., 2014b) in this study.

Once all the travel-time sensitivity kernels are calculated, smoothed, and interpolated, we can invert for the relative velocity perturbation field $\delta c(\mathbf{x})/c(\mathbf{x})$. As discussed in paper I, the relative velocity perturbation field $\delta c(\mathbf{x})/c(\mathbf{x})$ at each forward modeling grid node is linearly interpolated by its values at the eight neighboring inversion grid nodes. Based on the data distribution as shown in Fig. 2a, we setup the inversion

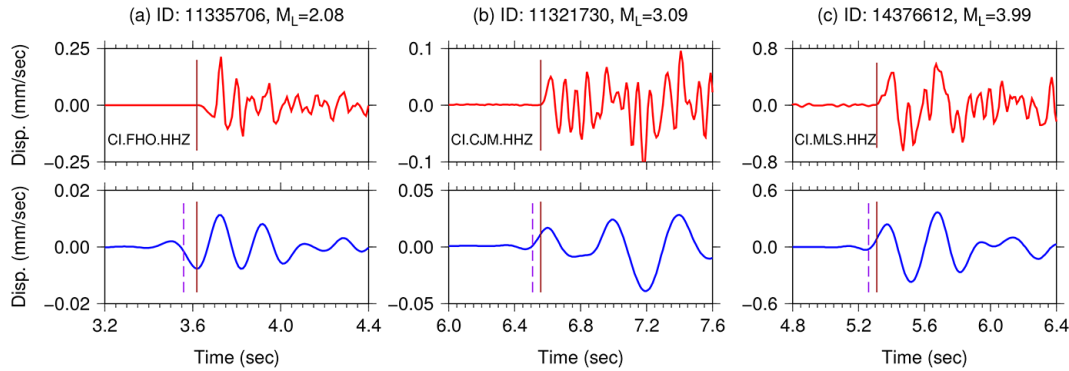


Figure 4. (a–c) Three examples of observed P wave arrival time picked on raw data obtained from the SCSN catalog (first row) and filtered seismograms filtered between 0.001 Hz and 5.0 Hz (second row). The brown lines denote the observed arrival-times T^{obs} determined by data analysts, and the dashed purple lines are the possible arrival-times $T^{\text{obs},f}$ manually picked on filtered seismograms. Earthquake IDs (such as 11335706), M_L magnitudes, and station names (such as CI.CJM) are specified for each record. The observed arrival times on raw data and on filtered seismograms are (a) $T^{\text{obs}} = 3.618$ s, $T^{\text{obs},f} \approx 3.558$ s, (b) $T^{\text{obs}} = 6.558$ s, $T^{\text{obs},f} \approx 6.508$ s, and (c) $T^{\text{obs}} = 5.311$ s, $T^{\text{obs},f} \approx 5.261$ s. The differences δt^f are less than 0.06 s.

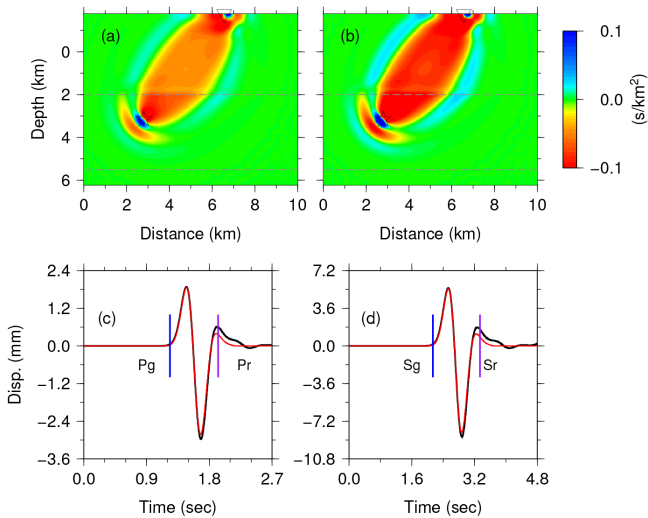


Figure 5. Panels **a** and **b** show examples of travel-time sensitivity kernels for the starting model m_1 of (a) the direct P wave (P_g) and (b) the direct S wave (S_g), which are fully separated from other later phases. The star and the inverse triangle indicate the earthquake at the depth of 3.14 km and a recording seismic station on the surface, respectively. The epicentral distance is 3.75 km. The dashed grey lines denote the velocity discontinuities at the depth of 2.0 km and 5.5 km. Panels **c** and **d** show the corresponding synthetic P wave and S wave seismograms (black curves). The arrival times of the direct waves (P_g and S_g) and reflected phases from the discontinuity at 5.5 km (P_r and S_r) are indicated by the blue and purple lines. The red waveforms are the windowed and tapered seismograms used to compute the travel-time sensitivity kernels of the direct arrivals shown in (a and b).

grid in the study area (Fig. 2b) with a horizontal grid spacing of 0.12° at the central portion and 0.15° near the edges (Fig. 2b), and seven vertical layers located at the depths of

1, 5, 10, 15, 21, 28, and 40 km. The spacing of the chosen inversion grid is much larger than that of the forward modeling grid. Additionally, the minimum wavelengths of both P and S waves are approximately half of the minimum inversion grid size. Generally speaking, at least four grid nodes per wavelength are needed to fully capture the seismic wavefield with a finite-difference forward modeling method (e.g., Yang et al., 2012; Tong et al., 2013). If an inverse algorithm has a resolving ability at the scale of the wavelength λ , such as that of full waveform inversion methods (Virieux and Operto, 2009), the grid spacing of the inversion grid should be at least 4 times that of the forward modeling grid spacing. Since the theoretical resolving ability of WETST is at the scale of $\sqrt{\lambda L}$ (L is the traveling distance) (Virieux and Operto, 2009), the grid spacing of the inverse grid should be even larger. Meanwhile, the resolution of the inversion results also relies on the coverage of seismic data. Checkerboard resolution tests are good measures on the resolving ability of an inverse algorithm with chosen seismic data and model parameterization. Therefore, checkerboard resolution tests are conducted to verify the chosen data, inversion grid, and the WETST algorithm in Sect. 3. However, due to the demanding computational cost, we do not test the limit of the inversion grid size in this study.

2.3 Inversion algorithm

After the calculation of sensitivity kernels and the interpolation of relative velocity perturbation $\delta c(\mathbf{x})/c(\mathbf{x})$ on inversion grid, tomographic Eq. (1) could be discretely expressed as a linear system $\mathbf{b} = \mathbf{A}\mathbf{X}$, where $\mathbf{b} = [b_m]_{M \times 1}$ is the travel-time residual vector ($b_m = T_m^{\text{obs}} - T_m^{\text{syn}}$ and m is the index for a particular travel-time record), $\mathbf{A} = [a_{m,n}]_{M \times N}$ is the Fréchet matrix, and $\mathbf{X} = [X_n]_{N \times 1}$ is the unknown velocity perturbation vector. Usually, the limited data coverage deems

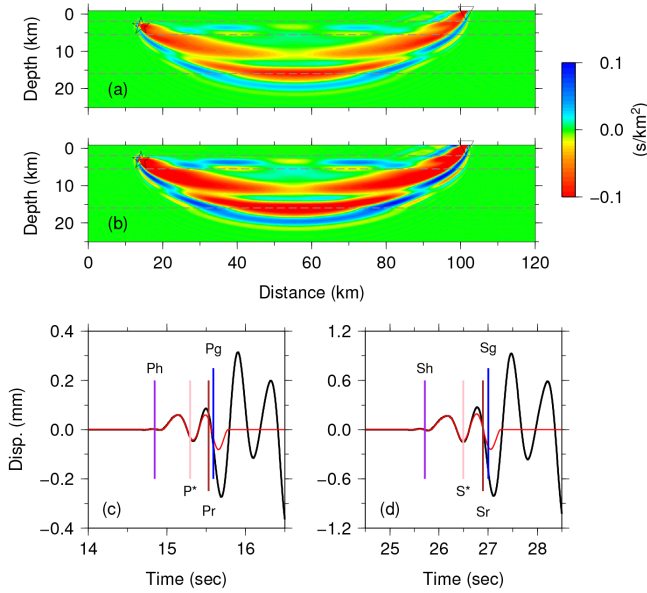


Figure 6. Panels **a** and **b** show examples of travel-time sensitivity kernels for the starting model m_1 of **(a)** the first arrival of P waves and **(b)** the first arrival of S waves. The earthquake is the same one as in Fig. 5 but the seismic station is at an epicentral distance of 87.24 km. In this case, the first arrivals are seismic waves refracted from the 5.5 km discontinuity but overlapped by other later phases. The dashed grey lines denote the velocity discontinuities at the depth 2.0 km and 5.5 km, and the Conrad discontinuity (16.0 km). Panels **c** and **d** show the corresponding synthetic P wave and S wave seismograms (black curves). The purple lines indicate the arrival times of the head waves refracted from the discontinuity at the depth of 5.5 km, the blue lines denote the onset times of the direct waves (Pg and Sg), the pink lines show the arrival times of the head waves refracted by the Conrad discontinuity, and the brown lines denote the arrival times of the reflected phases from the 5.5 km discontinuity (Pr and Sr). The red waveforms are the windowed and tapered seismograms used to compute the travel-time sensitivity kernels of the first arrivals shown in **(a)** and **(b)**.

this inversion an ill-posed problem, and $\mathbf{b} = \mathbf{A}\mathbf{X}$ is solved instead by minimizing the following regularized objective function

$$\chi(\mathbf{X}) = \frac{1}{2}(\mathbf{A}\mathbf{X} - \mathbf{b})^T \mathbf{C}_d^{-1}(\mathbf{A}\mathbf{X} - \mathbf{b}) + \frac{\epsilon^2}{2}\mathbf{X}^T \mathbf{C}_m^{-1}\mathbf{X} + \frac{\eta^2}{2}\mathbf{X}^T \mathbf{D}^T \mathbf{D}\mathbf{X}, \quad (7)$$

where \mathbf{D} is a first derivative smoothing operator, and ϵ and η are the damping parameter and the smoothing parameter, respectively (e.g., Tarantola, 2005; Li et al., 2008; Rawlinson et al., 2010a). \mathbf{C}_d and \mathbf{C}_m are the a priori data and model covariance matrices and reflect the uncertainties in the data and the initial model. Here we assume that both \mathbf{C}_d and \mathbf{C}_m are identity matrices.

Either the LSQR solver or non-linear conjugate-gradient method can be used to solve the optimization problem (Eq. 7)

as discussed in paper I (Paige and Saunders, 1982; Tromp et al., 2005; Tong et al., 2014b). We choose to use the LSQR solver in this study. The solution of the minimization problem (7) can be obtained by solving the equivalent linear system using the LSQR solver (Rawlinson et al., 2010a)

$$\begin{pmatrix} \mathbf{A} \\ \epsilon \mathbf{I} \\ \eta \mathbf{D} \end{pmatrix} \mathbf{X} = \begin{pmatrix} \mathbf{b} \\ 0 \\ 0 \end{pmatrix}. \quad (8)$$

The choice of the damping and smoothing parameters involves some degree of subjectivity. Analysis of the trade-off between the data variance reduction and the model smoothness may help the selection of optimal damping and smoothing parameters (Jiang et al., 2009; Tong et al., 2012). After the V_p and V_s models are updated, the Poisson's ratio (σ) image can be determined based on the relation

$$\frac{\delta\sigma}{\sigma} = \frac{2V_p^2 V_s^2}{(V_p^2 - 2V_s^2)(V_p^2 - V_s^2)} \left(\frac{\delta V_p}{V_p} - \frac{\delta V_s}{V_s} \right), \quad (9)$$

which is derived from the relation between Poisson's ratio and V_p/V_s ratio (Zhao et al., 1996)

$$\frac{V_p}{V_s} = \sqrt{\frac{2(1-\sigma)}{1-2\sigma}}. \quad (10)$$

Clearly, the reliability of the Poisson's ratio result depends on the accuracy of both recovered V_p and V_s structures.

3 Checkerboard resolution tests

We are ready to conduct wave-equation-based travel-time seismic tomography (WETST) based on the selected data, model parameterization, and inversion scheme laid out in previous sections. Prior to showing the tomographic results, we first examine the validity and reliability of this tomographic inversion based on checkerboard resolution tests. The checkerboard model is composed of alternating positive and negative velocity anomalies of 5% on the 3-D inversion grid nodes. Synthetic data are calculated for the checkerboard model based on 2-D finite-difference modeling. The starting velocity model is m_1 , i.e., the 1-D layered model with an undulated Moho as introduced in Sect. 2.2. The checkerboard patterns for both P and S wave velocity structures will be recovered through iterative procedures based on WETST.

3.1 Data variance vs. model variance trade-off analysis

In order to obtain the discrete velocity perturbation \mathbf{X} in Eq. (8) at each iteration, the damping parameter ϵ and the smoothing parameter η should be determined beforehand. In practice, these two parameters can be chosen via a trade-off analysis of data variance σ_d^2 and model variance σ_m^2 (Zhang

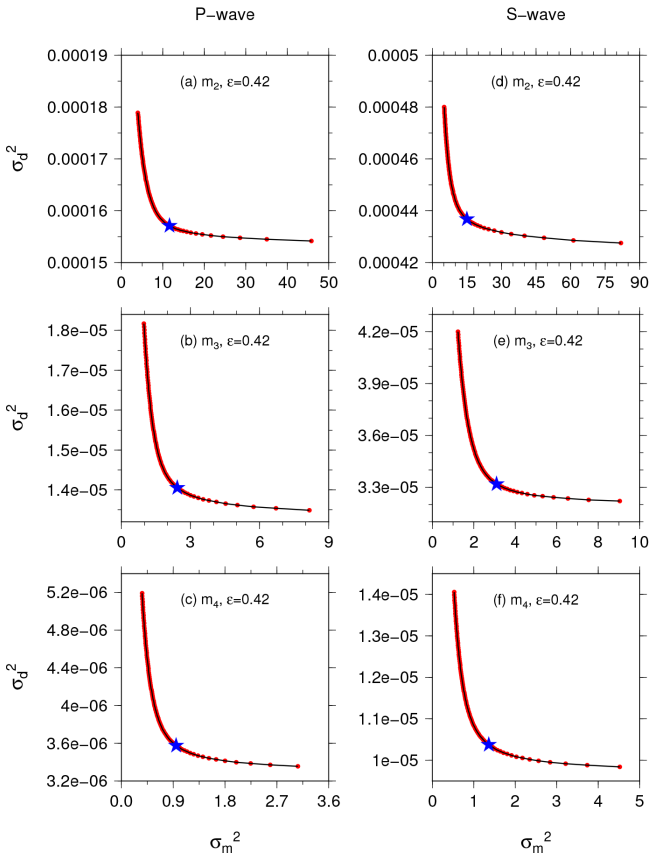


Figure 7. Trade-off analysis of data variance σ_d^2 and model variance σ_m^2 for damping parameters ϵ ranging from 0.1 (the rightmost red circle in each panel) to 2.0 (the leftmost red circle) with an interval of 0.02. Panels (a–c) show the trade-off curves of P wave checkerboard resolution tests for models m_2 – m_4 from the 1st, 2nd and 3rd iteration. Panels (d–f) are for S wave checkerboard tests. The blue star in each panel represents the values of model variance and data variance for the optimal damping parameter ϵ (values indicated in the same panel) for P wave or S wave at each iteration. The value of the unitless model variance σ_m^2 is at the scale of 10^{-4} .

et al., 2009). For the sake of computational efficiency, the unbiased data variance is approximated by

$$\sigma_d^2 \approx \frac{1}{M-1} \sum_{i=1}^M \left(T_i^{\text{obs}} - T_i^{\text{syn}} - \sum_{j=1}^N a_{ij} X_j - \bar{d} \right)^2, \quad (11)$$

where the data average \bar{d} is estimated as

$$\bar{d} = \frac{1}{M} \sum_{i=1}^M \left(T_i^{\text{obs}} - T_i^{\text{syn}} - \sum_{j=1}^N a_{ij} X_j \right). \quad (12)$$

The unbiased model variance σ_m^2 is calculated using the formula

$$\sigma_m^2 = \frac{1}{N-1} \sum_{i=1}^N (X_i - \bar{X})^2, \quad (13)$$

with $\bar{X} = \sum_{i=1}^N X_i / N$ is the mean of X . The trade-off analysis tries to find optimal damping and smoothing parameters that reduce most of the data variance without giving rise to too large model variance (Li et al., 2008; Zhang et al., 2009). For the checkerboard resolution tests, we search the damping parameter ϵ in the range [0.1, 2.0] with a step of 0.02, but set the smoothing parameter as $\eta = 0$ at each iteration to reflect the knowledge that the inverted structures are not smooth and have perturbations of opposite signs at neighboring nodes. Figure 7 shows the trade-off curves for both P wave and S wave checkerboard resolution tests at the first three iterations. Based on the L curve method (e.g., Calvetti et al., 2000; van Wijk et al., 2002; Zhang et al., 2009), we choose the optimal damping parameter ϵ for P wave or S wave test at each iteration near the corner of the corresponding trade-off curve. For example, to obtain the P wave velocity model m_2 from the starting model m_1 , the optimal damping parameter in Eq. (8) is chosen as $\epsilon = 0.42$ which gives the data variance $\sigma_d^2 = 1.571 \times 10^{-4} \text{ s}^2$ and model variance $\sigma_m^2 = 11.59 \times 10^{-4}$ (Fig. 7a). Note that the model variance is calculated with respect to the model in the previous iteration. Since the data variance is significantly reduced from model m_2 to m_4 and the value of the data variance in model m_4 is very small for either P wave or S wave checkerboard test (Fig. 7), we stop the iteration procedure at the fourth model m_4 .

3.2 Resolution results

Figures 8 and 9 show the iterative results of checkerboard tests at five representative layers in the crust for the P wave velocity (V_p) and S wave velocity (V_s) structures, respectively. Generally speaking, the checkerboard patterns are well resolved by WETST in the source area of the Landers earthquake. This indicates that both P wave and S wave data coverages are adequate enough, and the tomographic results inverted based on these data are reliable and can be used for further interpretation. More specifically, the checkerboard patterns at the five layers are almost recovered even at the first iteration (Fig. 8a–e and 9a–e), and the subsequent iterations only slightly refine the models (Fig. 8f–o and 9f–o). For both P wave and S wave tests, WETST has higher resolution in the upper crust (0–5.5 km) and middle crust (5.5–16.0 km) than that in the lower crust (> 16.0 km). This may be due to two main reasons. First, as most of the 2041 earthquakes used in this study are located above 20.0 km (Fig. 2a), the inversion grid nodes in the upper and middle crust are sampled by more data than those in the lower crust, which provides better constraints to the anomalies in the upper and middle crust. Secondly, the inversion grid nodes in the lower crust are mainly covered by travel-time sensitivity kernels for first arrivals at long epicentral distances as shown in Fig. 6. The resolving ability of the travel-time data is proportional to the width of the first Fresnel zone proportional to $\sqrt{\lambda L}$, where λ is the wavelength and L is the traveling distance (e.g., Wu and Toksoz, 1987; Virieux and Operto, 2009). A long trav-

Table 2. Structural similarity indices (SSIM) ζ between the checkerboard models and the iteratively updated inversion results (m_2 to m_4 , Figs. 8 and 9) at seven different depths for P wave and S wave checkerboard resolution tests.

Depth	1.0 km	5.0 km	10.0 km	15.0 km	21.0 km	28.0 km	40.0 km
P wave: model 2	0.8711	0.9175	0.9205	0.7437	0.6321	0.4186	0.5026
P wave: model 3	0.8569	0.9285	0.9300	0.8941	0.7343	0.4430	0.5013
P wave: model 4	0.9044	0.9402	0.9407	0.9225	0.7882	0.4674	0.5013
S wave: model 2	0.8831	0.9206	0.9206	0.7767	0.6652	0.3998	0.5052
S wave: model 3	0.8541	0.9245	0.9279	0.8901	0.7764	0.4347	0.5068
S wave: model 4	0.9047	0.9389	0.9416	0.9133	0.8199	0.4614	0.5060

Table 3. The root mean square (rms) values of P wave and S wave travel-time residuals in iteratively updated models.

rms	Model 1	Model 2	Model 3	Model 4
P wave	0.2540	0.1928	0.1754	0.1661
S wave	0.4724	0.3543	0.3196	0.3043

eling distance would result in relatively low resolution. In addition, the edges of the model range are likely to have poor resolution due to the lack of well crisscrossed kernels therein.

To further investigate the recovery ability of our tomographic method WETST, we calculate the structural similarity (SSIM) index ζ between the inverted model and the input checkerboard model (Tong et al., 2011, 2012). The SSIM index ζ between two velocity (or other positive physical parameter) models A and B is defined as

$$\zeta(A, B) = \frac{2\mu_A\mu_B\sigma_{AB}}{(\mu_A^2 + \mu_B^2)(\sigma_A^2 + \sigma_B^2)} + 0.5, \quad (14)$$

where μ_A , μ_B , σ_A , σ_B , and σ_{AB} are the average of A, average of B, variance of A, variance of B, and covariance of A and B, respectively. The 0.5 is added to ensure that SSIM index ζ is in the range [0.0, 1.0], and it is 1.0 only when A and B are identical (Tong et al., 2011). Table 2 shows the SSIM indices between the iteratively recovered P wave and S wave velocity models (m_2 to m_4 , Figs. 8 and 9) and the input checkerboard models at seven vertical layers. It can be observed that the SSIM indices at depths less than 21.0 km generally approach 1.0 through the iterations for both P wave and S wave tests. The recovery rates of the final P wave velocity and S wave velocity models m_4 are above 0.9 at the depths less than 21.0 km and greater than 0.78 at the depth of 21.0 km, again indicating that the heterogeneities from the surface to the depth of 21.0 km can be well resolved in this study. However, the SSIM indices at the depths 28 and 40 km are only around 0.5, implying decreased resolution in the lowermost crust and the uppermost mantle. It is worth noting that the SSIM indices at 1.0 km are smaller than those at 5.0, 10.0, and 15.0 km, which is probably caused by the better crisscrossing of the travel-time sensitivity kernels of earthquakes below 3.0 km at 5.0 km, 10.0 km, and 15.0 km depths than

that at 1.0 km depth (Figs. 5 and 6). The generally well-recovered V_p and V_s structures in our checkerboard resolution tests also imply that reliable Poisson’s ratio structures can be derived from this tomographic study. We have also conducted other checkerboard resolution tests for noise data, as summarized in the Supplement. All these resolution tests give us confidence that WETST should be able to generate high-resolution tomographic results for the source area of the Landers earthquake.

4 Tomographic inversions

4.1 Resolution parameters and models evaluation

The optimal regularization parameters ϵ and η should be determined to update the tomographic models at each iteration, similar to those in the checkerboard resolution tests. In this case, we search the optimal damping parameter ϵ in the range [6, 40] with an interval of 1 and the optimal smoothing parameter η over [2, 100] at a step of 2. In the searching procedure, we first set the smoothing parameter $\eta = 0$ and find the optimal damping parameter ϵ based on the L curve method. With the optimal damping parameter ϵ , we then determine the optimal smoothing parameter η in the searching region. For both P wave and S wave tomographic inversions, Fig. 10 shows the trade-off analysis of data variance σ_d^2 and model variance σ_m^2 along with different damping and smoothing parameters throughout the iterations. The optimal damping and smoothing parameters are also indicated in Fig. 10. After each model update, we compute the root mean square (rms) value of the travel-time residuals using the formula

$$\text{rms} = \sqrt{\frac{1}{M} \sum_{i=1}^M (T_i^{\text{obs}} - T_{i,k}^{\text{syn}})^2}, \quad (15)$$

where $T_{i,k}^{\text{syn}}$ is the arrival time of the i -th record in model m_k . Table 3 shows the values of rms. For both P wave and S wave results, we can find that rms monochronically decreases from m_1 to m_4 .

Figure 11 further shows the distributions of P wave (Fig. 11a–c) and S wave (Fig. 11d–f) travel-time residuals $T^{\text{obs}} - T^{\text{syn}}$ in models $m_1 - m_4$. It is clear that travel-time

residuals gradually become more centered around 0.0 s over iterations, indicating an overall reduction in total travel-time misfit. Since there is no significant decrease in rms (Table 3) from m_3 to m_4 , we stop our iteration at the fourth model for both P wave and S wave inversions, and m_4 is viewed as the final tomographic model used for interpretations in the following sections.

4.2 Tomographic images

We present iteratively updated map views of V_p (Fig. 12) and V_s (Fig. 13) models at five representative depths for the Landers earthquake area. It can be observed that the general patterns of V_p and V_s revealed by models $m_2 - m_4$ are almost the same, with only slight increase in the amplitudes of velocity anomalies over iterations (Figs. 12 and 13). This is consistent with the significant rms reduction from m_1 to m_2 , and minor reduction in the following updates, as shown in Table 3. However, it should be also noted that velocity anomalies near the boundaries of the study area become more clear over iterations, which agrees with the checkerboard resolution tests showing increased recovery from m_2 to m_4 (Table 2), especially in the boundary regions (Figs. 8 and 9). These results imply the necessity of iteratively improving the velocity models, even though the patterns of velocity anomalies could be almost recovered in the first iteration based on WETST with the LSQR solver.

We summarize the main features of the final tomographic model m_4 . Map views of V_p (Fig. 12k–o) and V_s (Fig. 13k–o) reveal large velocity variations of up to $\pm 8\%$, which indicate strong lateral heterogeneities in the model region. The epicentral areas of the Landers, Big Bear, and Joshua Tree earthquakes exhibit clear lateral velocity contrasts from the surface to about 15.0 km depth (Figs. 12k–n and 13k–n). In the Mojave block (Cheadle et al., 1986), north of the San Andreas fault, high V_p and V_s anomalies are generally visible at the shallow depth 1.0 km (Figs. 12k and 13k) and negative velocity perturbations exist in the middle crust (Figs. 12m, n and 13m, n). Similar depth variation of the velocity structures in this region was also reported by Zhou (2004). In the upper crust, low-velocity anomalies (Figs. 12k, l and 13k, l) exist along the San Andreas fault (SAF) and the San Jacinto fault (SJF) but only beneath the northwestern portion of the Elsinore fault (EF) (Hong and Menke, 2006). Additionally, a significant high-velocity zone is visible between the SAF and the SJF, which results in strong velocity contrasts across the two faults near the surface (Allam and Ben-Zion, 2012; Lin, 2013). The high-velocity zone between the EF and the north portion of the SJF may indicate a reversal in the velocity contrast polarity along the SJF at around 5.0 km depth (Figs. 12l and 13l) (Allam and Ben-Zion, 2012). In the middle crust, the SAF, the SJF, and the EF roughly show relatively high-velocity anomalies (Figs. 12m, n and 13m, n) (Lin et al., 2007). However, in the lower crust (21.0 km), low-velocity anomalies are generally reported along these fault systems

(Figs. 12o and 13o). We will discuss this low-velocity feature in detail in the next section. Beneath the Salton Trough (ST), which is a sediment-filled graben near the southern part of the SAF (Allam and Ben-Zion, 2012), a pronounced low V_p and V_s anomaly exists in the upper crust (Figs. 12k, l and 13k, l), and high P wave velocity structures are revealed in the middle and lower crust (Fig. 12m–o). This is consistent with the results of Allam and Ben-Zion (2012).

A series of vertical cross-sectional views from the surface to 40 km depth for V_p , V_s , and Poisson's ratio σ structures are shown in Figs. 14 and 15. Since both V_p and V_s structures are almost well recovered in the crust (Figs. 8 and 9 and Table 2), Poisson's ratio models in Figs. 14c, f, i and 15c, f, i can be viewed as being reliably determined based on Eq. (9). Note that the map views of the iteratively updated Poisson's ratio σ structure are included in the Supplement (Figs. S3–S5). Figure 14 shows three cross sections along the profiles through the hypocenters of the Landers earthquake, the Joshua Tree earthquake, the Big Bear earthquake, and the 1999 Hector Mine earthquake where profile AB is nearly parallel to the fault zone of the Landers earthquake. It can be observed that the Landers mainshock is located in a high-velocity, low Poisson's ratio anomaly (Fig. 14a–c and g–i). Additionally, the hypocenters of the Joshua Tree, Big Bear, and 1999 Hector Mine earthquakes are at or near high-velocity and low Poisson's ratio anomalies (Fig. 14). By inverting P wave arrival times from aftershocks of 1992 southern California earthquakes, Lees and Nicholson (1993) also reported that high V_p anomalies occur at or near nucleation sites of the Joshua Tree, Landers, and Big Bear mainshocks. Both velocity and Poisson's ratio structures change drastically around the source areas of the Landers mainshock and the other three large earthquakes. Material properties of the source areas of the four large earthquakes are consistent with those of the brittle seismogenic layer, which is characterized by high velocity and low Poisson's ratio (Wang et al., 2008). A prominent feature of the vertical cross sections along profiles CD and EF is the low V_p , low V_s , and high Poisson's ratio structure to the west of the Big Bear mainshock hypocenter in the lower crust (Fig. 14d–i), which has been interpreted as a ductile and weak region (Zhao and Kanamori, 1993; Zhao et al., 2005). A low-velocity and high Poisson's ratio structure is also visible in the lower crust close to the hypocenter of the Landers mainshock (Fig. 14a–c and g–i). In addition, tomographic results and seismicity along the profile AB confirm the conclusion of Lin et al. (2007) that shallow earthquakes mostly occurred in high V_p regions and mid-crustal earthquakes occurred in low V_p zones. Seismicity along profile AB is mainly the aftershocks of the Landers earthquake (Fig. 14a–c), and it can be observed that to the south of the Landers mainshock hypocenter, seismicity strikes across the Joshua Tree aftershock zone, extends about 40.0 km south of the epicenter of the Landers mainshock, and terminates within a few kilometers of the SAF. Immediately following that of the Salton Trough, a low-velocity and high Poisson's

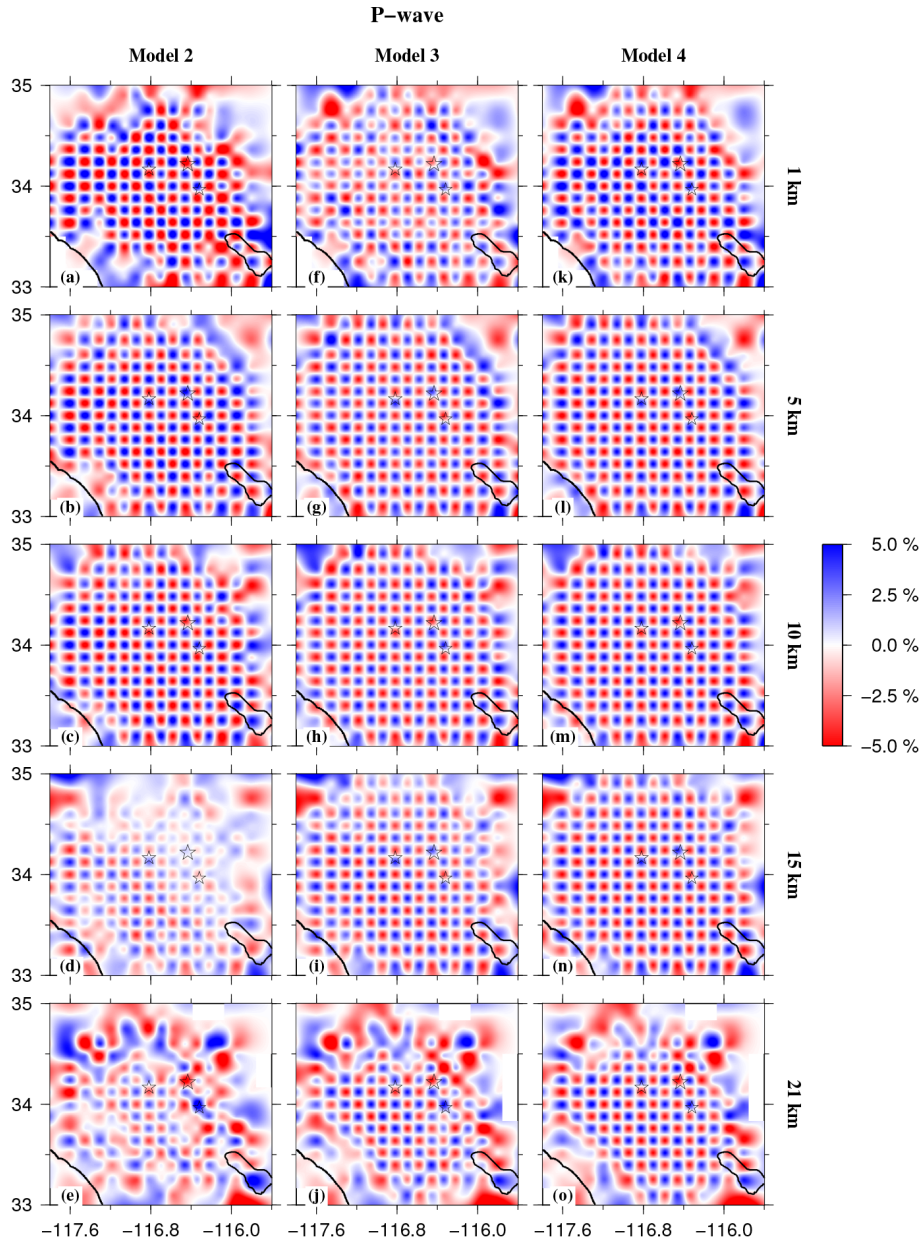


Figure 8. Iterative results m_2 (a–e), m_3 (f–j), and m_4 (k–o) of a checkerboard resolution test for P wave velocity structure at five representative depth layers (1.0, 5.0, 10.0, 15.0, and 21.0 km). Red and blue colors denote low- and high-velocity perturbations, respectively. The velocity perturbation in percentage scale is shown at the right hand side. The stars denote the epicentral locations of the Landers, the Joshua Tree, and the Big Bear earthquakes.

ratio anomaly exists near the surface (Zhao and Kanamori, 1993). Additionally, to the north of the Landers mainshock, aftershocks extend about 60.0 km to the Camp Rock fault and are surrounded by low-velocity and high Poisson’s ratio rocks beneath them (Hauksson et al., 1993; Zhao and Kanamori, 1993).

Figure 15 shows the vertical cross sections along the Elsinore fault (EF), the San Jacinto fault (SJF), and the San Andreas fault (SAF). Beneath the northwest segment of the EF,

a low-velocity and high Poisson’s ratio anomaly is visible in the upper and middle crust, underlain by a high-velocity and low Poisson’s ratio structure (Fig. 15a–c). These are contrary to the structural properties under the central and southeast sections of the EF, which generally exhibit high velocity and low Poisson’s ratio in the upper and middle crust and low-velocity and high Poisson’s ratio beneath (Fig. 15a–c). Seismicity along the EF is generally focused between 5.0 km and 15.0 km. Velocity and Poisson’s ratio models reveal complex

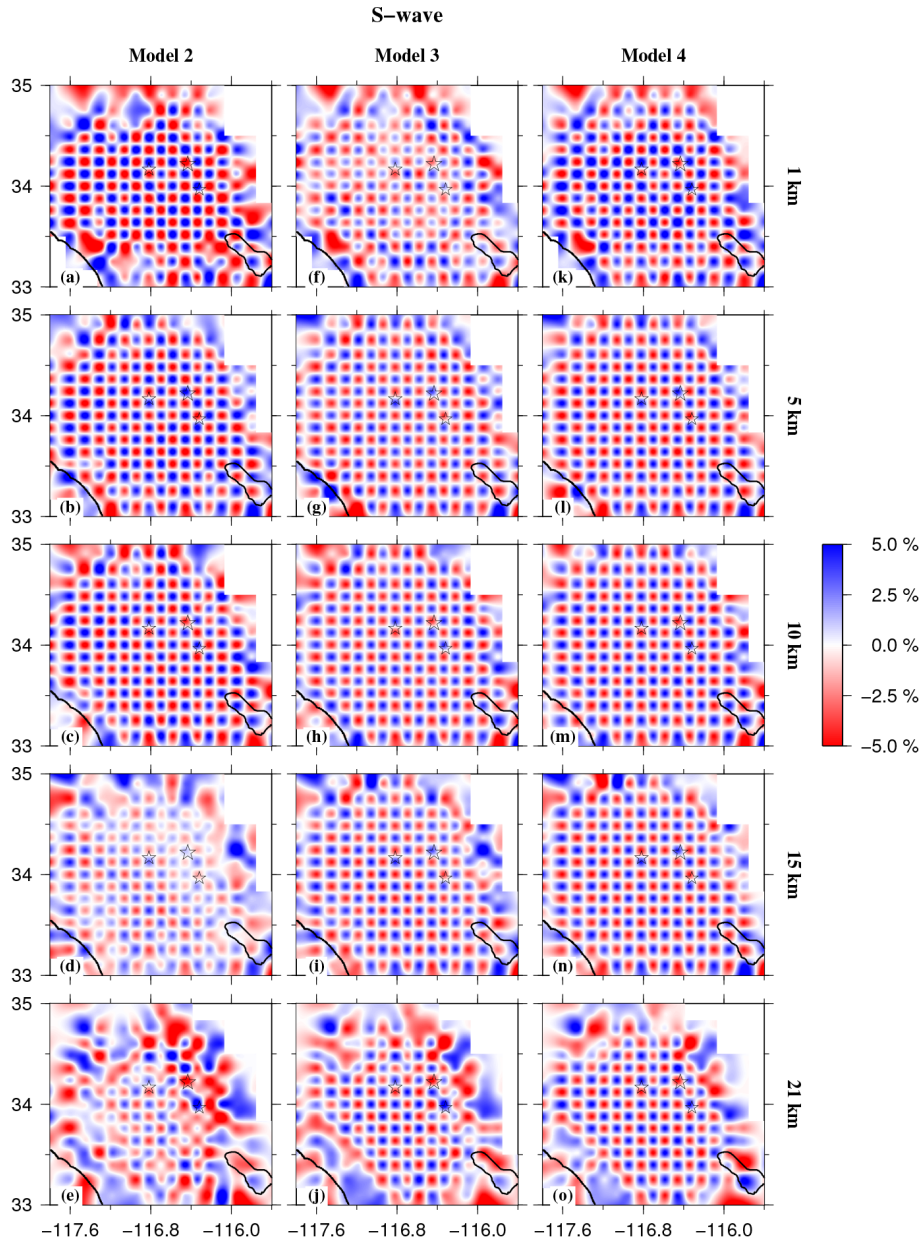


Figure 9. The same as Fig. 8 but for S wave velocity structure.

patterns beneath both the SJF and the SAF (Fig. 15d–i). Alternating high- and low-velocity variations can be observed along the faults near the surface, which can be interpreted as manifestations of the complex surface geological patterns. However, along both the SJF and the SAF, we can observe a layer with low velocity and high Poisson’s ratio at the depth of about 5.0 km. Right beneath this layer, high-velocity and low Poisson’s ratio structures exist in the middle crust. Seismicity along the SJF and the SAF mainly occurred in this high-velocity and low Poisson’s ratio region. Additionally, the seismicity along the SJF is much more active than that along the SAF for study area (Lin, 2013). The lower crust

is generally dominated by low-velocity and high Poisson’s ratio structures. Specifically, near the southeast sections of the SJF and the SAF which are close to the Salton Trough, there are mainly low-velocity and high Poisson’s ratio structures at shallow depths and high-velocity and low Poisson’s ratio anomalies in the middle and lower crust. These features are consistent with the extension and crustal thinning of the Salton Trough region (Allam and Ben-Zion, 2012).

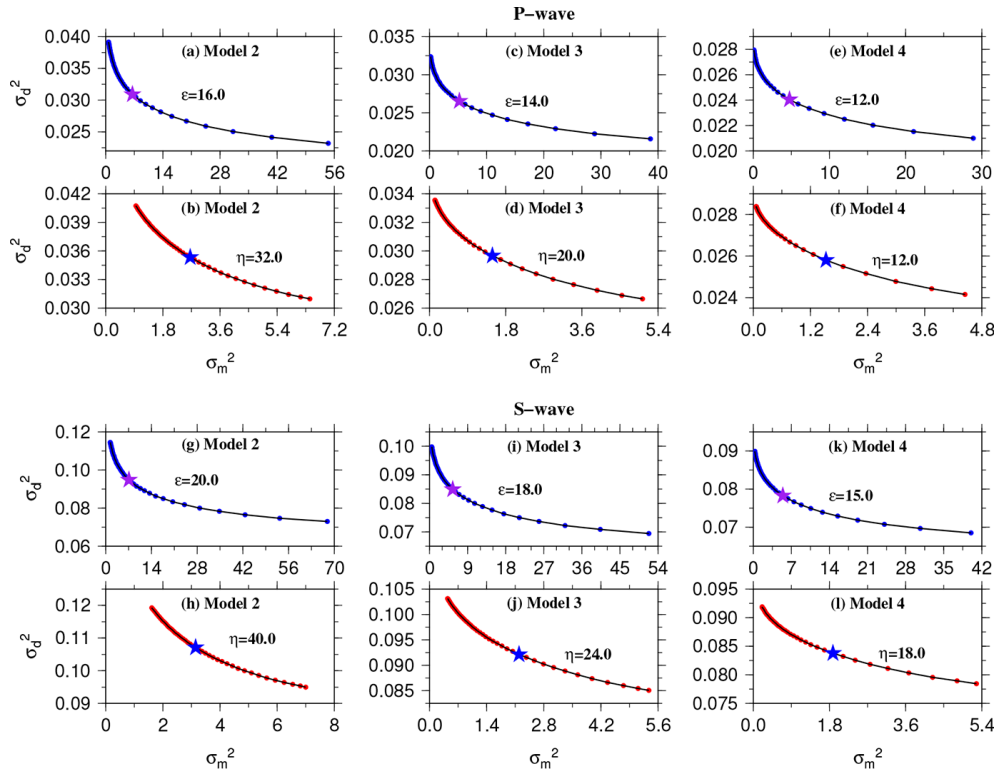


Figure 10. Trade-off analysis of data variance σ_d^2 and model variance σ_m^2 for 35 damping values equally in [6.0, 40.0] and 50 smoothing values over [2, 100.0] with an interval of 2.0 at each iteration to obtain *P* wave (a–f) and *S* wave (g–l) models $m_2 - m_4$. By setting the smoothing parameter $\eta = 0.0$, the optimal damping parameter ϵ is first determined based on the *L* curve method as shown in (a), (c), (e), (g), (i), and (k) at each iteration. The purple stars highlight the values of data variance σ_d^2 and model variance σ_m^2 calculated with the optimal damping parameters. The optimal smoothing parameter η is then determined with the corresponding optimal damping parameter also based on the *L* curve method in (b), (d), (f), (h), (j), and (l). The blue stars are at the crosses determined by the values of data variance σ_d^2 and model variance σ_m^2 calculated with the optimal damping and smoothing parameters. The value of the unitless model variance σ_m^2 is at the scale of 10^{-4} .

5 Discussion and conclusions

Our new tomographic models in general agreement with the results of previous studies for overlapped research regions (e.g., Zhao and Kanamori, 1993; Zhou, 2004; Tian et al., 2007b; Tape et al., 2009; Lin et al., 2010; Allam and Ben-Zion, 2012). As shown in Figs. 12 and 13, the tomographic models have mainly four typical features. (1) Strong lateral heterogeneities (up to $\pm 8\%$) exist in the crust (e.g., Zhao et al., 1996; Tape et al., 2009), which reflects complex compositional, structural, and petrophysical variations. Since crustal heterogeneities undoubtedly affect seismic wave propagation (Tape et al., 2009), an accurate forward modeling technique is essential for correctly capturing the interactions between seismic waves and heterogeneous structures. This indicates the necessity of solving full wave equations in complex structure imaging. (2) Significant lateral velocity contrasts can be observed in the epicentral areas of the Landers, Big Bear, and the Joshua Tree earthquakes from the surface to the middle crust and also across the San Jacinto fault and the San Andreas fault near the surface (Al-

lam and Ben-Zion, 2012). (3) The velocity structures in the upper crust correlate well with the surface geological features (Zhao et al., 1996; Tian et al., 2007b; Lin, 2013). For example, due to the fractured rocks within the fault zones and the thick sedimentary materials (Tian et al., 2007b), low-velocity anomalies are prominent along the San Andreas fault and the San Jacinto fault, near the coast, and beneath the Salton Trough in the upper crust (Figs. 12k, l and 13k, l). (4) Pronounced low-velocity anomalies are recovered along the Elsinore fault, the San Jacinto fault, and the San Andreas fault in the lower crust. Because of their poor resolution in the lower crust, this feature was not reported by previous crustal tomographic studies that also used only first arrival-time data (e.g., Lin et al., 2007; Tian et al., 2007a). Contrary to that, our tomographic results have satisfactory recovery rates at 21.0 km depth and clearly reveal these low-velocity anomalies (Figs. 12o and 13o). The adjoint tomography of the southern California crust (Tape et al., 2009) shows visible but less significant low *S* wave velocity anomalies along the three faults at 20.0 km depth. By combining earthquake

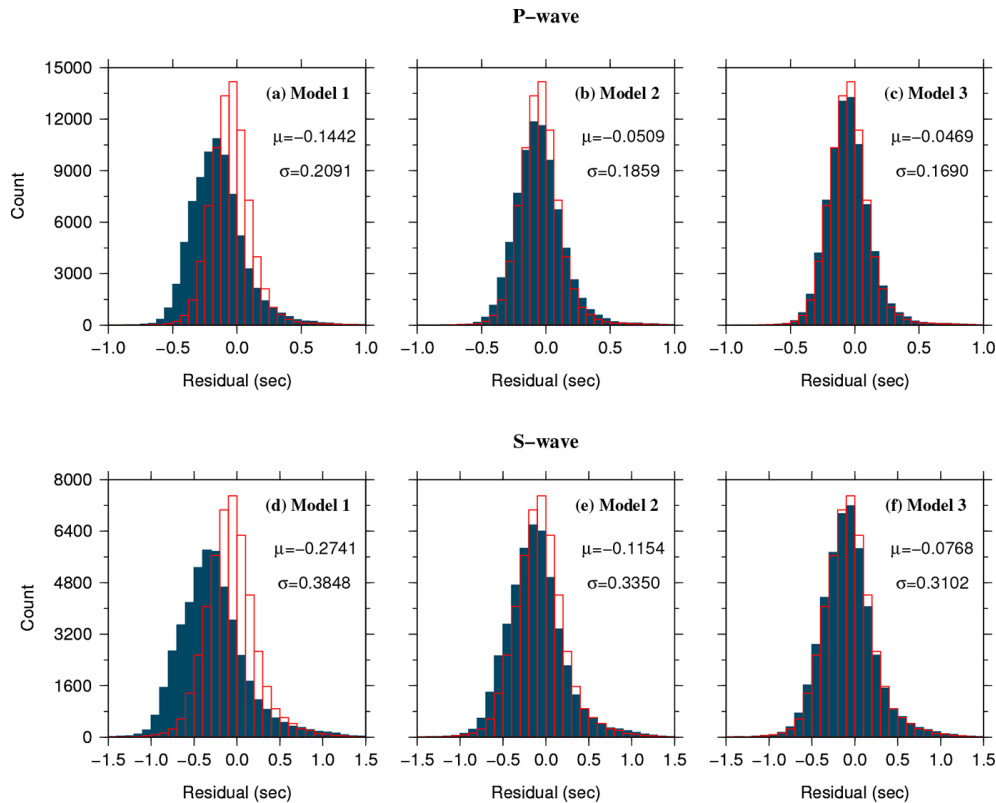


Figure 11. *P* wave (a–c) and *S* wave (d–f) travel-time residuals $T^{\text{obs}} - T^{\text{syn}}$ in models $m_1 - m_3$ (blue histograms) compared to those in model m_4 (red histograms). The mean μ and standard deviation σ of the travel-time residuals in models $m_1 - m_3$ (corresponding to blue histograms) are shown in each panel. In m_4 , the mean and standard deviation values of the *P* wave travel-time residuals are $\mu = -0.0457$ s and $\sigma = 0.1596$ s, and those of the *S* wave travel-time residuals are $\mu = -0.0652$ s and $\sigma = 0.2972$ s.

recordings and ambient-noise cross-correlation phase measurements, stacking of station-to-station correlations of ambient seismic noise by incorporating receiver function analysis with gravity and magnetic data, Lee et al. (2013) also discovered the low-velocity anomalies in the lower crust of southern California with full 3-D waveform tomographic inversions. Hussein et al. (2012) proposed that a magmatic intrusion at a depth of about 20 km exists in the southwest of Salton Sea. It extends for 70 km in the SW–NE direction and may imply the existence of fluids (Hussein et al., 2012). Since their reported magmatic intrusion zone is partially within our study area and appears to be covered by low-velocity anomalies, it may be possible to associate the low-velocity anomalies in the lower crust with the existence of crustal fluids.

Seismicity in the study area mainly occurred in the regions with high velocity and low Poisson’s ratio, which can be associated with the brittle seismogenic layers (Wang et al., 2008). Particularly, the seismic rupture zone in the upper crust around the Landers earthquake fault zone (Fig. 14a–c) generally shows high V_p , high V_s , and relatively low Poisson’s ratio (Zhao and Kanamori, 1993). Zhao and Kanamori (1995) suggested that high-velocity areas are generally con-

sidered to be strong and brittle parts of the fault zone, which are capable of generating earthquakes. In contrast, low-velocity regions may represent the regions of either higher degree of fracture, high fluid pressure, or higher temperatures where deformations are more likely to be aseismic. In addition, a closer observation reveals that the mainshocks of the Landers earthquake (M_w 7.3) and other three strong earthquakes with magnitudes greater than 6.0 (the Joshua Tree, Big Bear, and Hector Mine earthquakes) occurred very close to the boundaries of high V_p , high V_s and low Poisson’s ratio anomalies (Fig. 14). Indeed, many large crustal earthquakes occurred in regions with significant seismic property variations, such as the 2008 M_w 7.2 Iwate–Miyagi earthquake (Cheng et al., 2011) and the 2011 M_w = 7.0 Iwaki earthquake (Tong et al., 2012). While the Iwate–Miyagi earthquake and the Iwaki earthquake have been hypothesized to be caused by fluid dehydration from the subducting Pacific plate (e.g., Wang et al., 2008; Cheng et al., 2011; Tong et al., 2012), Tian et al. (2007b) concluded that fluids from long-term infiltration of surface water may have triggered large earthquakes in the Landers source area.

Seismic properties along the San Andreas fault, the San Jacinto fault and the Elsinore fault are also explored in this

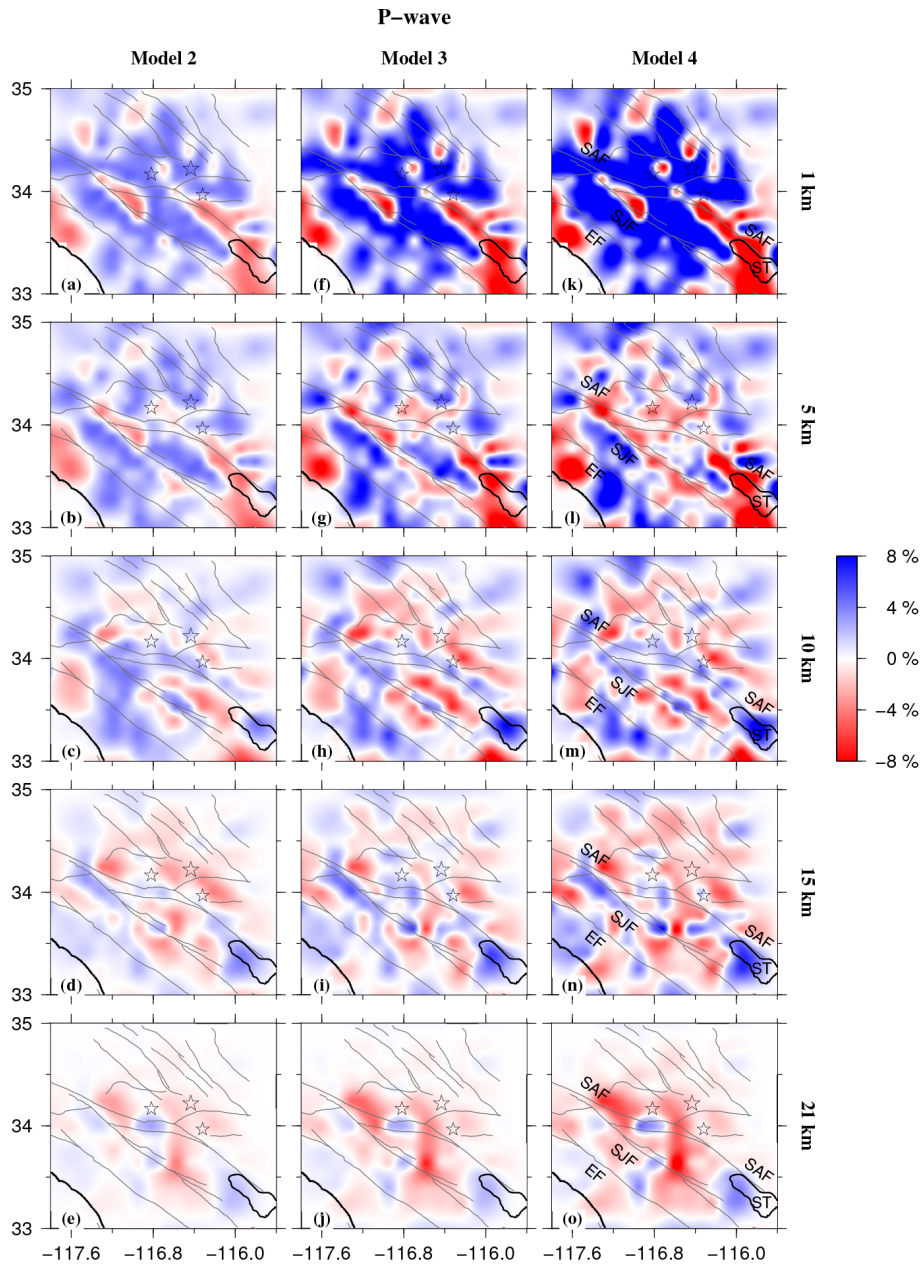


Figure 12. Map views of the *P* wave tomography at five representative depths for models m_2 (left column), m_3 (middle column), and m_4 (right column). The layer depth is shown just on the right hand side of each row. Red and blue colors denote low and high velocities, respectively. The velocity perturbation scale (in percent) is also shown. On each map, grey lines denote active faults, and the empty stars indicate the epicentral locations of the Landers earthquake, the Big Bear earthquake, and the Joshua Tree earthquake (Fig. 1). SAF is the short form for the San Andreas fault, SJF is the San Jacinto fault, EF is the Elsinore fault, and ST is the Salton Trough.

study. Velocity and Poisson’s ratio structures in the upper crust show very complex patterns along the three faults. These near surface features are associated with key fault properties such as rheology, brittle–ductile transition, pore pressure, stress, geotherm, and rupture energy (e.g., Li and Vernon, 2001; Hong and Menke, 2006). High-velocity and low Poisson’s ratio structures are generally observed in the middle crust along the three faults. Additionally, seismic-

ity also mainly distributes in this region. In the lower crust, we generally observe low-velocity and high Poisson’s ratio structures except around the area near the Salton Trough. Since the width of fault zones ranges from tens to hundreds meters while the lateral inversion grid spacing is about 10.0 km, it is difficult to obtain detailed fault structures in this regional tomographic study. A detailed discussion on the structures of the San Jacinto and the Elsinore fault zones can

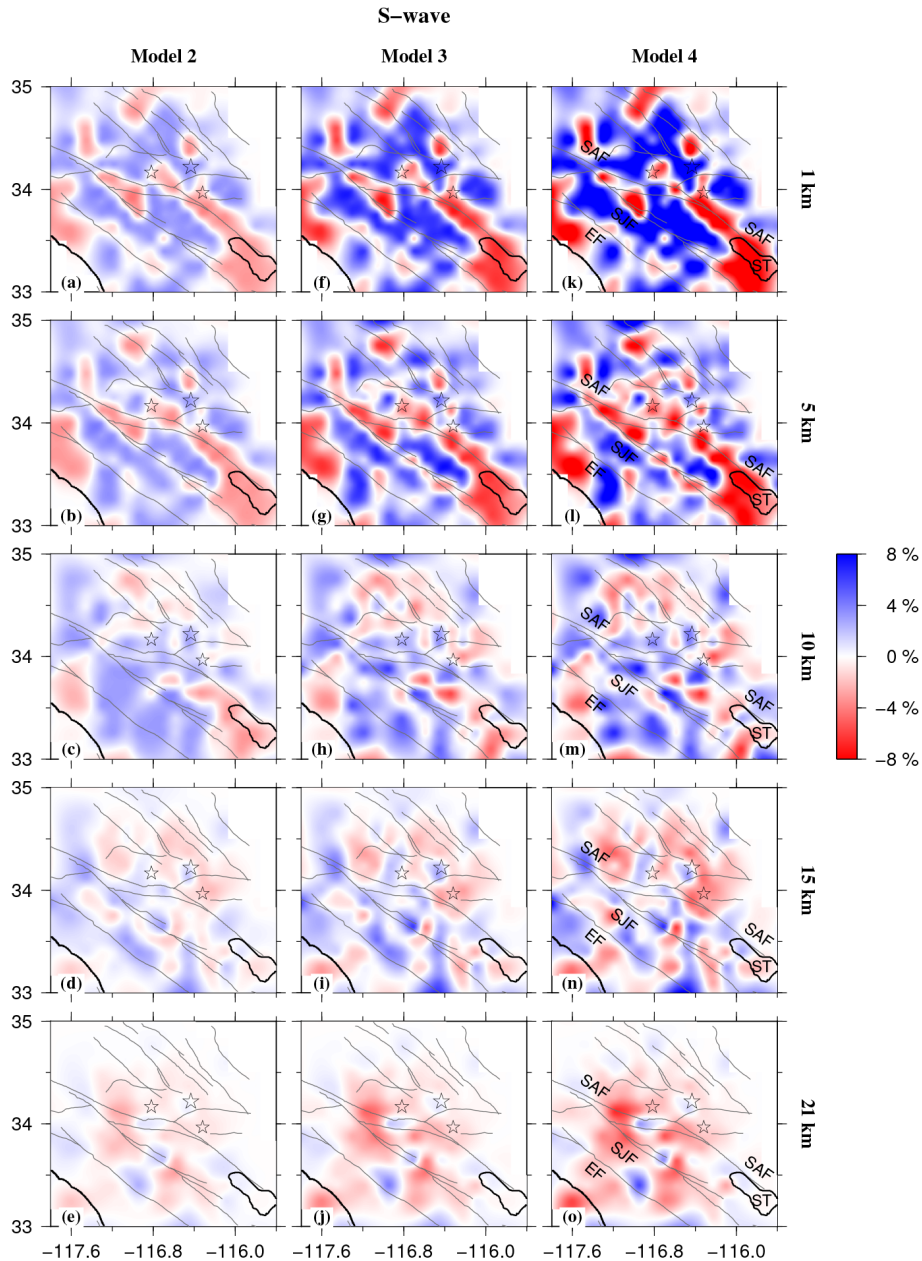


Figure 13. The same as Fig. 12 but for *S* wave tomography.

be found in Hong and Menke (2006) which used local seismic records for clustered fault-zone earthquakes for imaging.

Based on the above discussions, we conclude that the crustal structures beneath the 1992 Landers earthquake (M_w 7.3) source area have been successfully imaged based on the wave-equation-based travel-time seismic tomography (WETST) technique. The recovered strong crustal heterogeneities advocate the use of more subtle full wave-equation solvers in tomographic imaging to accurately simulate seismic wave propagation in complex media. As our forward modeling is restricted in a 2-D plane and based on an ef-

ficient high-order central difference method, WETST only requires moderate computational resources even when individual kernels for each source–receiver pair are constructed. For example, a total of about 10 000 CPU hours are used to generate the *P* wave and *S* wave tomographic results in this work, much fewer than 0.8 million hours used by the adjoint tomography of the southern California crust in Tape et al. (2009). These properties suggest that WETST can be used to reveal the structures of the Earth’s interior quickly when large data sets are involved for further applications. Of course, the underlying 2-D acoustic wave-equation approx-

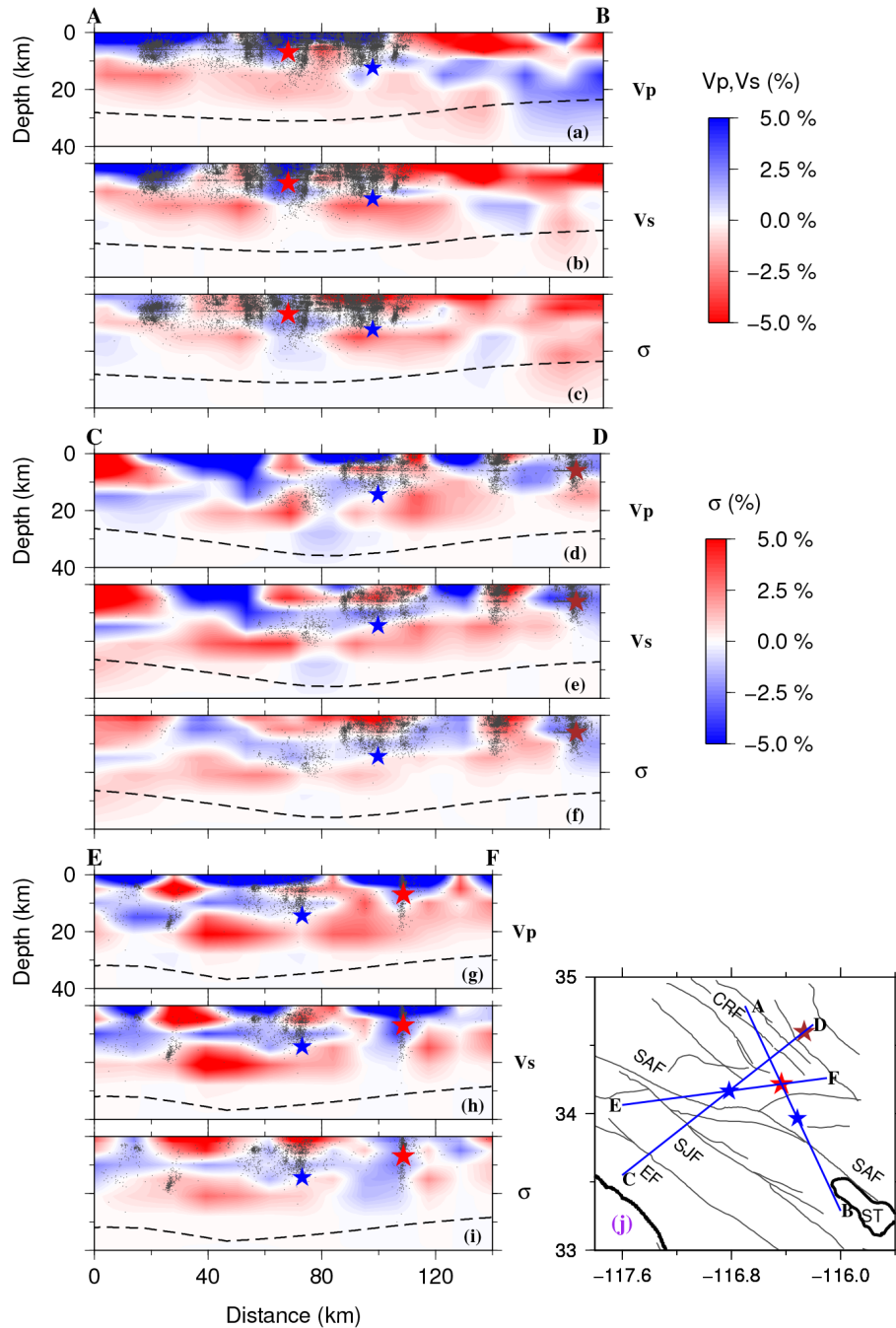


Figure 14. Vertical cross sections of *P* wave velocity, *S* wave velocity, and Poisson’s ratio images (m_4) along profile AB (a–c), CD (d–f) and EF (g–i) as indicated on the inset map (j). Low velocity and high Poisson’s ratio are shown in red color, while high velocity and low Poisson’s ratio are represented by blue color. The scales for the velocity and Poisson’s ratio σ perturbations (in %) are shown on the right. Small grey dots denote events with magnitudes greater than 1.5 between January 1992 and November 2013 that are located within 3.0 km width along each profile. The hypocenters for the Landers mainshock (M_w 7.3) hypocenter at 7.0 km depth and the Hector Mine earthquake at 6.0 km are shown by the red and brown star, respectively. The hypocenters for the Joshua Tree earthquake at 12.4 km and the Big Bear earthquake at 14.4 km are indicated by blue stars. The dashed lines represent the Moho discontinuity obtained by Zhu and Kanamori (2000). CRF is short for the Camp Rock fault, also indicated on the inset map (j).

imation for the forward modeling ignores the effect of off-plane structures. To what extent is this kind of approximation

valid should be further investigated and will be part of our future work. However, as it is still computationally expensive to

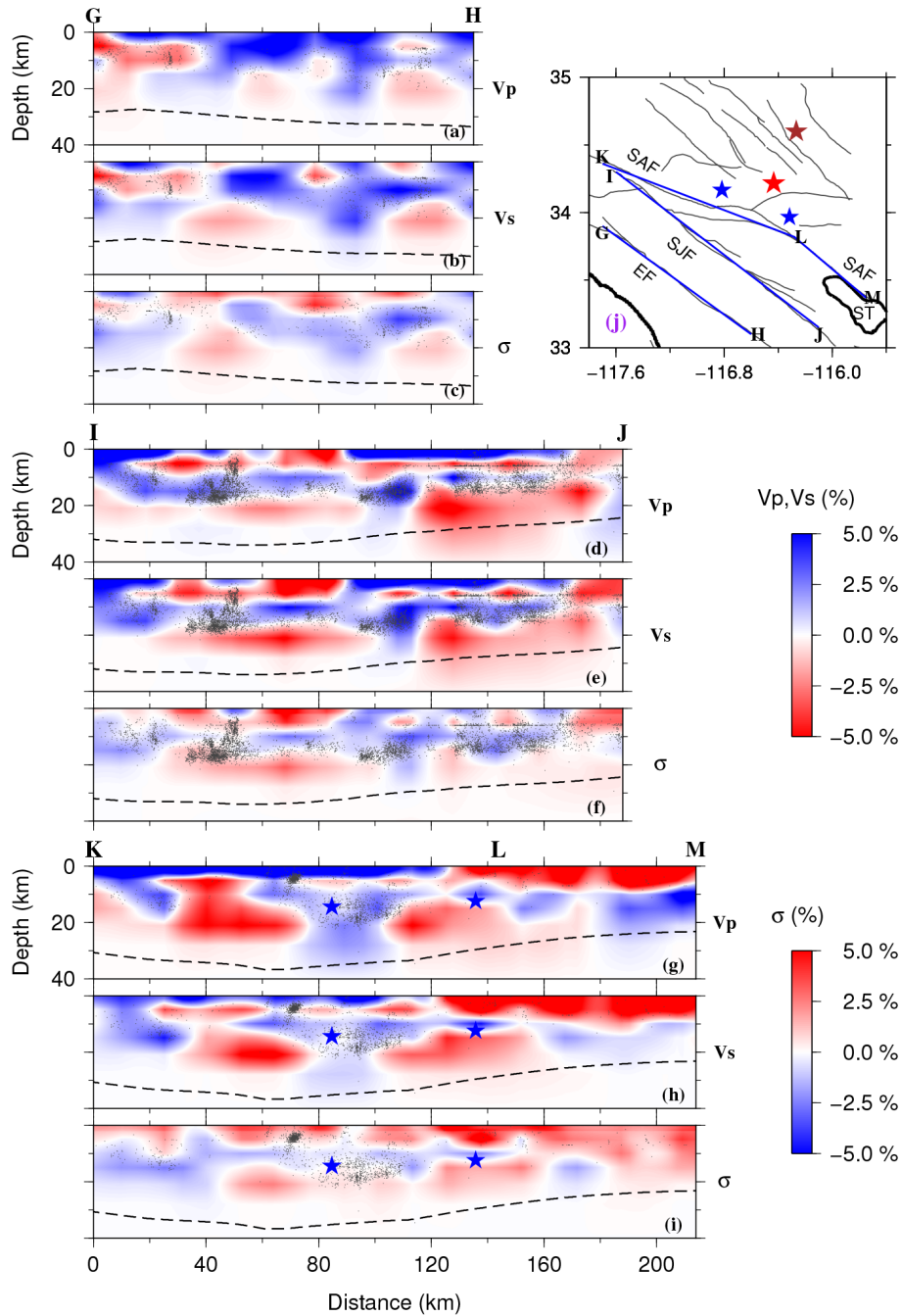


Figure 15. The same as Fig. 14 but along the Elsinore fault (EF), the San Jacinto fault (SJF) and the San Andreas fault (SAF), denoted by cross sections GH (a–c), IJ (d–f) and KLM (g–i), respectively.

calculate individual kernels for the “3-D–3-D” tomographic method (e.g., Tape et al., 2010; Tong et al., 2014a, c), WETST may serve as a bridge between the conventional but the most widely used ray-based tomographic methods and the promising “3-D–3-D” adjoint tomography based upon full 3-D numerical solvers of the seismic wave equation (Liu and Gu, 2012).

The Supplement related to this article is available online at doi:10.5194/se-14-1169-2014-supplement.

Acknowledgements. We thank the Southern California Earthquake Data Center for providing the high-quality arrival-time data used in this study. This work is supported by NSERC through the G8 Research Councils Initiative on Multilateral Research Grant and the Discovery Grant (no. 487237), Japan Society for the Promotion of Science (Kiban-S 11050123), and National Natural Science Foundation of China (grant no. 41230210). X. Yang was partially supported by the Regents Junior Faculty Fellowship of University of California, Santa Barbara. Numerical simulations and inversions are performed on workstations acquired through combined funding of Canada Foundation for Innovation (CFI), Ontario Research Fund (ORF), and University of Toronto Startup. All figures are made with the Generic Mapping Tool (GMT) (Wessel and Smith, 1991). We thank K. Liu and two anonymous reviewers for providing constructive comments and suggestions that improved the manuscript.

Edited by: K. Liu

References

- Allam, A. A. and Ben-Zion, Y.: Seismic velocity structures in the southern California plate-boundary environment from double-difference tomography, *Geophys. J. Int.*, 190, 1181–1196, 2012.
- Aochi, H. and Fukuyama, E.: Three-dimensional nonplanar simulation of the 1992 Landers earthquake, *J. Geophys. Res.*, 107, 1–4, 2002.
- Calvetti, D., Morigi, S., Reichel, L., and Sgallari, F.: Tikhonov regularization and the L curve for large discrete ill-posed problems, *J. Comput. Appl. Math.*, 123, 423–446, 2000.
- Cheadle, M. J., Czuchra, B. L., Byrne, T., Ando, C. J., Oliver, J. E., Brown, L. D., and Kaufman, S.: The deep crustal structure of the Mojave Desert, California, from COCORP seismic reflection data, *Tectonics*, 5, 293–320, 1986.
- Cheng, B., Zhao, D., and Zhang, G.: Seismic tomography and anisotropy in the source area of the 2008 Iwate-Miyagi earthquake (M 7.2), *Phys. Earth Planet. In.*, 184, 172–185, 2011.
- Fichtner, A., Bunge, H. P., and Igel, H.: The adjoint method in seismology I. Theory, *Phys. Earth Planet. In.*, 157, 86–104, 2006.
- Frey Mueller, J., King, N. E., and Segall, P.: The coseismic slip distribution of the Landers earthquake, *B. Seismol. Soc. Am.*, 84, 646–659, 1994.
- Gautier, S., Nolet, G., and Virieux, J.: Finite-frequency tomography in a crustal environment: application to the western part of the Gulf of Corinth, *Geophys. Prospect.*, 56, 493–503, 2008.
- Hauksson, E., Jones, L. M., Hutton, K., and Eberhart-Phillips, D.: The 1992 Landers earthquake sequence: Seismological observations, *J. Geophys. Res.*, 98, 19835–19858, 1993.
- Hong, T.-K. and Menke, W.: Tomographic investigation of the wear along the San Jacinto fault, southern California, *Phys. Earth Planet. In.*, 155, 236–248, 2006.
- Hussein, M., Velasco, A. A., Serpa, L., and Doser, D.: The role of fluids in promoting seismic activity in active spreading centers of the Salton Trough, California, USA, *Int. J. Geosci.*, 3, 303–313, 2012.
- Jiang, G., Zhao, D., and Zhang, G.: Seismic tomography of the Pacific slab edge under Kamchatka, *Tectonophysics*, 465, 190–203, 2009.
- Lee, E., Chen, P., Jordan, T., Maechling, P., Denolle, M., and Beroza, G.: Full-3-D waveform tomography of Southern California crustal structure by using earthquake recordings and ambient noise Green's functions based on adjoint and scattering-integral methods, Abstract, in: 2013 Fall Meeting, AGU, 2013.
- Lees, J. and Nicholson, C.: Three-dimensional tomography of the 1992 southern California sequence: constraints on dynamic earthquake rupture?, *Geology*, 21, 385–388, 1993.
- Li, C., van der Hilst, R. D., Engdahl, E. R., and Burdick, S.: A new global model for P wave speed variations in Earth's mantle, *Geochem. Geophys. Geos.*, 9, Q05018, doi:10.1029/2007GC001806, 2008.
- Li, Y. G. and Vernon, F. L.: Characterization of the San Jacinto fault zone near Anza, California by fault zone trapped waves, *J. Geophys. Res.*, 106, 30671–30688, 2001.
- Lin, G.: Three-dimensional seismic velocity structure and precise earthquake relocations in the Salton Trough, southern California, *B. Seismol. Soc. Am.*, 103, 2694–2708, 2013.
- Lin, G., Shearer, P. M., Hauksson, E., and Thurber, C. H.: A three-dimensional crustal seismic velocity model for southern California from a composite event method, *J. Geophys. Res.*, 112, B11306, doi:10.1029/2007JB004977, 2007.
- Lin, G., Thurber, C. H., Zhang, H., Hauksson, E., Shearer, P. M., Waldhauser, F., Brocher, T. M., and Hardebeck, J.: A California statewide three-dimensional seismic velocity model from both absolute and differential times, *B. Seismol. Soc. Am.*, 100, 225–240, 2010.
- Liu, Q. and Gu, Y. J.: Seismic imaging: from classical to adjoint tomography, *Tectonophysics*, 566–567, 31–66, 2012.
- Liu, Y. and Schuster, G. T.: Wave-equation traveltimes inversion, *Geophysics*, 56, 645–653, 1992.
- Olsen, K. B., Madariaga, R., and Archuleta, R. J.: Three-dimensional dynamic simulation of the 1992 Landers earthquake, *Science*, 278, 834–838, 1997.
- Paige, C. and Saunders, M.: LSQR: an algorithm for sparse linear equations and sparse least-squares, *Trans. Maths Software*, 8, 43–71, 1982.
- Parsons, T. and Dreger, D. S.: Static-stress impact of the 1992 Landers earthquake sequence on nucleation and slip at the site of the 1999 $M = 7.1$ Hector Mine earthquake, southern California, *Geophys. Res. Lett.*, 27, 1949–1952, 2000.
- Peyrat, S., Olsen, K., and Madariaga, R.: Dynamic modeling of the 1992 Landers earthquake, *Geophys. Res. Lett.*, 106, 26467–26482, 2001.
- Rawlinson, N., Pozgay, S., and Fishwick, S.: Seismic tomography: a window into deep Earth, *Phys. Earth Planet. In.*, 178, 101–135, 2010a.
- Rawlinson, N., Sambridge, M., and Hauser, J.: Multipathing, reciprocal traveltimes fields and raylets, *Geophys. J. Int.*, 181, 1077–1092, 2010b.
- Sieh, K., Jones, L., Hauksson, E., Hudnut, K., Eberhart-Phillips, D., Heaton, T., Hough, S., Hutton, K., Kanamori, H., Lilje, A., Lind-

- vall, S., McGill, S. F., Mori, J., Rubin, C., Spotila, J. A., Stock, J., Thio, H. K., Treiman, J., Wernicke, B., and Zachariassen, J.: Near-field investigations of the Landers earthquake sequence, April to July 1992, *Science*, 260, 171–176, 1993.
- Tape, C., Liu, Q., and Tromp, J.: Finite-frequency tomography using adjoint methods – methodology and examples using membrane surface waves, *Geophys. J. Int.*, 168, 1105–1129, 2007.
- Tape, C., Liu, Q., Maggi, A., and Tromp, J.: Adjoint tomography of the southern California crust, *Science*, 325, 988–992, 2009.
- Tape, C., Liu, Q., Maggi, A., and Tromp, J.: Seismic tomography of the southern California crust based on spectral-element and adjoint methods, *Geophys. J. Int.*, 180, 433–462, 2010.
- Tarantola, A.: *Inverse Problem Theory and Methods for Model Parameter Estimation*, 1st edn., Society for Industrial and Applied Mathematics, Philadelphia, 2005.
- Thurber, C. H.: Earthquake locations and three-dimensional crustal structure in the Coyote Lake area, central California, *J. Geophys. Res.*, 88, 8226–8236, 1983.
- Tian, Y., Zhao, D., Sun, R., and Teng, J.: The 1992 Landers earthquake: effect of crustal heterogeneity on earthquake generation, *Chinese J. Geophys.*, 50, 1300–1308, 2007a.
- Tian, Y., Zhao, D., and Teng, J.: Deep structure of southern California, *Phys. Earth Planet. In.*, 165, 93–113, 2007b.
- Tong, P., Zhao, D., and Yang, D.: Tomography of the 1995 Kobe earthquake area: comparison of finite-frequency and ray approaches, *Geophys. J. Int.*, 187, 278–302, 2011.
- Tong, P., Zhao, D., and Yang, D.: Tomography of the 2011 Iwaki earthquake (M 7.0) and Fukushima nuclear power plant area, *Solid Earth*, 3, 43–51, doi:10.5194/se-3-43-2012, 2012.
- Tong, P., Yang, D. H., Hua, B. L., and Wang, M. X.: A high-order stereo-modeling method for solving wave equations, *B. Seismol. Soc. Am.*, 103, 811–833, 2013.
- Tong, P., Chen, C.-W., Komatitsch, D., Basini, P., and Liu, Q.: High-resolution seismic array imaging based on an SEM-FK hybrid method, *Geophys. J. Int.*, 197, 369–395, 2014a.
- Tong, P., Zhao, D., Yang, D., Yang, X., Chen, J., and Liu, Q.: Wave-equation based traveltimes seismic tomography – Part 1: Method, *Solid Earth*, 5, 1–18, doi:10.5194/se-5-1-2014, 2014b.
- Tong, P., Komatitsch, D., Tseng, T.-L., Hung, S.-H., Chen, C.-W., Basini, P., and Liu, Q.: A 3D spectral-element and frequency-wavenumber (SEM-FK) hybrid method for high-resolution seismic array imaging, *Geophys. Res. Lett.*, 41, 7025–7034, doi:10.1002/2014GL061644, 2014c.
- Tromp, J., Tape, C., and Liu, Q.: Seismic tomography, adjoint methods, time reversal and banana-doughnut kernels, *Geophys. J. Int.*, 160, 195–216, 2005.
- Unruh, J. R., Lettis, W. R., and Sowers, J. W.: Kinematic interpretation of the 1992 Landers earthquake, *B. Seismol. Soc. Am.*, 84, 537–546, 1994.
- van Wijk, K., Scales, J. A., Navidi, W., and Tenorio, L.: Data and model uncertainty estimation for linear inversion, *Geophys. J. Int.*, 149, 625–632, 2002.
- Virieux, J. and Operto, S.: An overview of full waveform inversion in exploration geophysics, *Geophysics*, 74, WCC1–WCC26, 2009.
- Wang, Z., Fukao, Y., Kodaira, S., and Huang, R.: Role of fluids in the initiation of the 2008 Iwate earthquake (M7.2) in northeast Japan, *Geophys. Res. Lett.*, 35, L24303, doi:10.1029/2008GL035869, 2008.
- Wessel, P. and Smith, W. H. F.: Free software helps map and display data, *EOS T. Am. Geophys. Un.*, 72, 441–448, 1991.
- Wu, R. S. and Toksoz, M. N.: Diffraction tomography and multi-source holography applied to seismic imaging, *Geophysics*, 52, 11–25, 1987.
- Yang, D., Tong, P., and Deng, X.: A central difference method with low numerical dispersion for solving the scalar wave equation, *Geophys. Prospect.*, 60, 885–905, 2012.
- Zhang, H., Sarkar, S., Toksoz, M. N., Kuleli, H. S., and Al-kindy, F.: Passive seismic tomography using induced seismicity at a petroleum field in Oman, *Geophysics*, 74, WCB57–WCB69, 2009.
- Zhao, D.: Multiscale seismic tomography and mantle dynamics, *Gondwana Res.*, 15, 297–323, 2009.
- Zhao, D. and Kanamori, H.: The 1992 Landers earthquake sequence: earthquake occurrence and structural heterogeneities, *Geophys. Res. Lett.*, 20, 1083–1086, 1993.
- Zhao, D. and Kanamori, H.: The 1994 Northridge earthquake : 3-D crustal structure in the rupture zone and its relation to the, *Geophys. Res. Lett.*, 22, 763–766, 1995.
- Zhao, D., Hasegawa, A., and Horiuchi, S.: Tomographic imaging of *P* and *S* wave velocity structure beneath northeastern Japan, *J. Geophys. Res.*, 97, 19909–19928, 1992.
- Zhao, D., Kanamori, H., and Humphreys, E.: Simultaneous inversion of local and teleseismic data for the crust and mantle structure of southern California, *Phys. Earth Planet. In.*, 93, 191–214, 1996.
- Zhao, D., Todo, S., and Lei, J.: Local earthquake reflection tomography of the Landers aftershock area, *Earth Planet. Sc. Lett.*, 235, 623–631, 2005.
- Zhou, H.: Multi-scale tomography for crustal *P* and *S* velocities in southern California, *Pure Appl. Geophys.*, 161, 283–302, 2004.
- Zhu, L. and Kanamori, H.: Moho depth variation in southern California from teleseismic receiver functions, *J. Geophys. Res.*, 105, 2969–2980, 2000.